Phase field modeling of hydraulic fracturing with interfacial damage in highly heterogeneous fluid-saturated porous media

Liang Xia, Julien Yvonnet, Siavash Ghabezloo

Phase field modeling of hydraulic fracturing with interfacial damage in highly heterogeneous fluid-saturated porous media

L. Xia [a,b], J. Yvonnet [a,*] S. Ghabezloo [c]

[a] *Université Paris-Est, Laboratoire Modélisation et Simulation Multi Échelle MSME UMR 8208 CNRS, 5 bd Descartes, 77454 Marne-la-Vallée, France.*

[b] *The State Key Laboratory of Digital Manufacturing Equipment and Technology, Huazhong University of Science and Technology, Wuhan, China*

[c] *Université Paris-Est, Laboratoire Navier, CNRS UMR 8205, ENPC, IFSTTAR, 6/8 avenue Blaise Pascal, 77455 Marne-la-Vallée, France.*

Abstract

In this work, we propose an extension of the phase field model for the modeling of hydraulic fracturing or cracking in heterogeneous saturated porous media. The involved extensions comprise: (a) taking into account interfacial damage between the inclusions and the matrix; (b) modeling fluid flow within both matrix cracks and interfacial cracks; (c) the possibility to handle geometries of the heterogeneous media in the form of regular grids of voxels e.g. as obtained from experimental imaging techniques. The developed numerical framework is based on the phase field method with a regularized description of both bulk and interface discontinuities, extended to a fully coupled hydro-mechanical framework. Both 2D and 3D examples are presented for hydro-mechanical microcracking initiation and propagation in voxel-based models of complex heterogeneous media with interfacial damage between the inclusions and the matrix.

Key words: Hydraulic fracturing; Phase field method; Crack propagation; Heterogeneous materials; Voxel-based models

* Correspondance to J. Yvonnet
Email address: julien.yvonnet@univ-paris-est.fr (J. Yvonnet).

1 Introduction

The computational modeling of fracturing in fluid-saturated porous media is of essential importance for numerous practical applications in geotechnical, environmental, petroleum engineering and biomechanics. Typical applications include the caprock integrity during the geological gas storage [47], nuclear waste disposal and hydraulic fracturing for oil and gas extraction. The computational modeling of hydraulic fracturing has attracted a special research attention due to the growing interest of the petroleum industry (see e.g. [3]). To optimize the hydraulic fracturing processing so as to maximize the extraction while preventing potential environmental contamination, developing an efficient and robust numerical methods for the modeling of the hydraulic fracturing processing is of primary importance.

Attempts to provide analytical solutions for the hydraulic fracturing problem can be found e.g. in [24,48,16,14,25]. The earliest work on numerical modeling of hydraulic fracturing can be traced back to Boone and Ingraffea [6], who combined the finite element method and the finite difference method to solve the poroelasticity problem, where the fracture was modeled by a cohesive zone on an assumed crack path. Since then, several methods have been developed to simulate the hydraulic fracturing or crack propagation in fluid-saturated porous media such as the cohesive zone model, adaptive meshing strategies [45,46], approaches based on lattice, particle models, or discrete elements [12,51,19,52,20,43], extended finite element method (XFEM) for geometrically linear setting [13,44,37,36,21], or XFEM for nonlinear setting at finite strains [23].

An alternative simulation approach to fracture, namely the phase field method proposed by Francfort and Marigo [15], Bourdin et al. [8], Hakim and Karma [22], Miehe et al. [32,28], Borden et al. [7] (only to name a few) has shown promising computational advantages in handling very complex crack topologies and has been recently adapted in a multi-physics framework (see e.g. [31,27,29,54,9]). In this context, the sharp crack discontinuities are regularized by a diffuse phase field approximation within a continuum formulation, making it very flexible to handle crack nucleation, multiple crack fronts, cracks merging and branching in both 2D and 3D without ad hoc numerical treatment (see e.g., Nguyen et al. [41,40,39]). The phase field approach to fracture is consistent with brittle fracture through variational methods based on energy minimization as shown in [15]. This technique has been applied for the first time by Chukwudozie et al. [11] to hydraulic fracturing with the assumption of linear elastic and impermeable matrix. Phase field hydraulic fracturing of fluid-saturated porous media has been recently developed by Wheeler et al. [53] and Mikelić et al. [33,34] within the Biot's geometrically linear framework at small strains. More recently, Miehe et al. [30,29] have introduced a full

variational framework for phase field fracture within a geometrically nonlinear framework of poroelasticity at finite strains [5].

The above mentioned contributions dedicated to phase field modeling of hydraulic fracturing all assume a homogeneous porous medium that can be macroscopically represented using Biot's theory. However, several potential applications of fracture due to pressurized water imply heterogeneous media. In [35,26], the effects of heterogeneities in phase field hydraulic fracture models were taken into account by local variations of mechanical properties. The most obvious application of fluid driven fracture in the presence of *aggregate-type* inclusions concerns the petroleum engineering and the unconventional oil and gas production in shale formations by hydraulic fracturing. The microstructure of oil and gas shales generally consists of a clayey matrix and inclusions of various minerals, including quartz and calcite. Another potential application concerns the safety analysis of nuclear waste disposal in claystones (similar microstructure as shales). The temperature increase resulting from the storage of high activity nuclear waste leads to a thermal pressurization of the pore fluid in the low permeability claystone, mainly due to the discrepancy between the thermal expansion coefficients of the pore fluid and the one of the porous matrix [17]. In fact the thermal expansion of water is almost one order of magnitude higher than the one of most solids. A temperature increase in a low permeability fluid saturated porous material results in a short term pore pressure increase, which can potentially yield to initiation and propagation of cracks in the claystone host rock, which similar to the shales, is composed of a clayey matrix and different mineral inclusions [4]. A similar phenomenon of thermal pressurization of the pore fluid can occur in cement based materials and concrete structures, as for example in nuclear waste disposal projects when the waste is covered by cement based materials or in the concrete structure of nuclear reactors. The cement paste has a particularly high thermal pressurization coefficient [18] and a quite low permeability. Therefore, a temperature increase results in a pore pressure increase and can potentially lead to generation and propagation of cracks. One may also think of similar thermal pressurization phenomenon in concrete subjected to fire.

In this work, we propose an extension of the phase field model for the modeling hydraulic fracturing or cracking in heterogeneous saturated porous media. The involved extensions comprise: (a) taking into account interfacial damage between the inclusions and the matrix; (b) modeling fluid flow within both matrix cracks and interfacial cracks; (c) the possibility to handle geometries of the heterogeneous media in the form of regular grids of voxels e.g. as obtained from experimental imaging techniques. The developed numerical framework employs the phase field method with a regularized description of both bulk and interface cracks, extended to a fully coupled hydro-mechanical framework. More specifically, the generalized Biot's linear theory has been adopted to model the deformable porous media combined with phase field fracture mod-

eling and interfacial damage. The discontinuous crack topology is regularized by a continuous phase field and its evolution is driven by a threshold-based criterion in terms of the effective stress related to the solid skeleton of a fluid-saturated porous medium. The jumps at the interfaces between the porous matrix and the inclusions are also described by a regularized approximation. Displacement jumps result in additional anisotropic permeability for the assumed of Poiseuille-type fluid flow within the fracture. Note that in our framework the fluid can pass within the matrix cracks as well as within interface cracks.

The paper is organized as follows. In section 2, we introduce diffuse approximations for cracks and interface using the phase field method. In section 3, the phase field modeling of hydraulic fracturing with interfacial damage in heterogeneous media within the Biot's macroscopic continuum framework is presented. Section 4 provides the space-time discretization strategy and the staggered solution scheme for the updates of the crack phase field and the coupled displacement-pressure problems. Finally, we validate in section 5 the proposed method by benchmark tests and practical examples involving interfacial cracking in pixel/voxel-based models of heterogeneous media.

2 Diffuse approximation of discontinuous fields

Let $\Omega \in \mathbb{R}^D$ be an open domain $D = 2, 3$ describing a heterogeneous medium composed of a homogeneous porous matrix embedding elastic inclusions. The external boundary of Ω is denoted by $\partial\Omega \in \mathbb{R}^{D-1}$. The internal interfaces between the porous medium and the inclusions are collectively denoted by Γ^I. Cracks which may propagate in the porous medium and pass through the interfaces as depicted in Fig. 1 are collectively denoted by Γ. In this work, we adopt the framework proposed in [38,1,32] for a regularized representation of discontinuities extended to interfaces as in [42]. In this regularized framework, the cracks are approximately represented by a scalar phase field $d(\mathbf{x}, t)$ and the interfaces by a fixed scalar function $\beta(\mathbf{x})$.

2.1 Phase field approximation of bulk cracks

The scalar crack phase field $d(\mathbf{x}, t)$ can be determined through solving the following boundary value problem subjected to Dirichlet boundary conditions

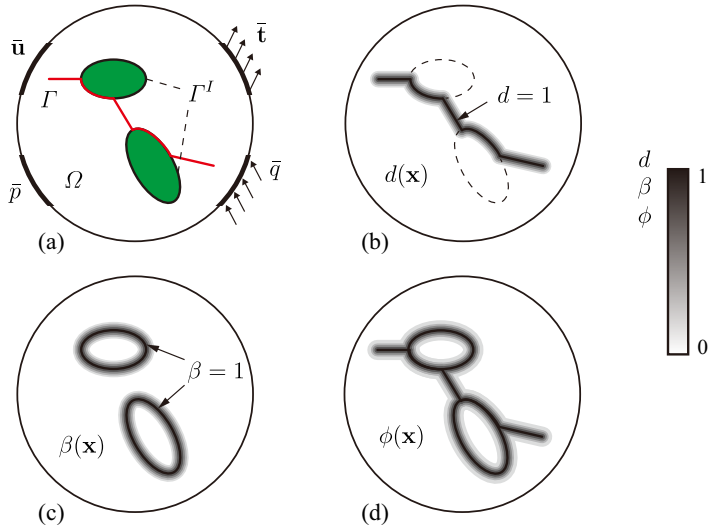

Fig. 1. Diffused approximation of cracks and interfaces: (a) a porous medium containing two inclusions and a crack passing through the interfaces; (b) diffuse representation of the crack by the field $d(\mathbf{x})$; (c) smeared representation of the interfaces by the field $\beta(\mathbf{x})$ and (d) indicator function $\phi(\mathbf{x})$.

$d = 1$ on the crack (see [32] for more details):

$$\begin{cases} d(\mathbf{x},t) - \ell_d^2 \nabla^2 d(\mathbf{x},t) = 0, \quad \text{in } \Omega \\ d(\mathbf{x},t) = 1, \quad \text{on } \Gamma \\ \nabla d(\mathbf{x},t) \cdot \mathbf{n} = 0 \quad \text{on } \partial\Omega, \end{cases} \tag{1}$$

where $\nabla^2(.)$ is the Laplacian operator, ℓ_d is a length scale parameter that governs the width of the regularization zone and gives for $\ell_d \to 0$ the exact sharp crack in (1) Γ in (1), and $\mathbf{n}$ is the unit outward normal vector to $\partial\Omega$. In the following, we denote the crack phase field $d(\mathbf{x},t)$ by d to alleviate the notations. It has been shown that the system of equations (1) corresponds to the Euler-Lagrange equation associated with the variational problem:

$$d = \text{Arg}\left\{\inf_{d \in S_d} \Gamma_d(d)\right\}, \qquad \Gamma_d(d) = \int_\Omega \gamma_d(d)\, \mathrm{d}V, \tag{2}$$

where $S_d = \{d | d(\mathbf{x}) = 1, \forall \mathbf{x} \in \Gamma\}$, and γ_d is the crack surface density function per unit volume defined by:

$$\gamma_d(d) = \frac{1}{2\ell_d} d^2 + \frac{\ell_d}{2} \nabla d \cdot \nabla d. \tag{3}$$

The functional $\Gamma_d(d)$ represents the total length of the crack in 2D and the total crack surface area in 3D. A detailed explanation of (3) can be found in [32].

It is worth noting that in (3), ℓ_d does not represent physically the exact opening (displacement jump) of the crack, which can take different values at different points of the cracks, but a parameter which is used to regularize the discontinuities. It has been shown (see e.g. [2,40]) that this parameter can be related to other material parameters like the maximum tensile stress and can then be identified as a material parameter e.g. by inverse approaches [39], and then does not physically represents the crack width. The opening displacement across the crack within this regularized framework will be defined in Eq. (11) in the following.

2.2 Phase field approximation of interfaces

The diffuse approximation of damageable interfaces was introduced in [42]. The scalar interface function $\beta(\mathbf{x})$ is determined in the same manner as $d(\mathbf{x}, t)$ by solving the boundary value problem subjected to Dirichlet conditions $\beta = 1$ on the interfaces:

$$\begin{cases} \beta(\mathbf{x}) - \ell_\beta^2 \nabla^2 \beta(\mathbf{x}) = 0, & \text{in } \Omega \\ \beta(\mathbf{x}) = 1, & \text{on } \Gamma^I \\ \nabla\beta(\mathbf{x}) \cdot \mathbf{n} = 0, & \text{on } \partial\Omega, \end{cases} \tag{4}$$

where ℓ_β is a length scale parameter that governs the width of the regularization zone of the interface. Similarly, Eqs (4) corresponds to the Euler-Lagrange equation of the variational problem:

$$\beta = \text{Arg}\left\{ \inf_{\beta \in S_\beta} \Gamma_\beta(\beta) \right\} \quad \text{with} \quad \Gamma_\beta(\beta) = \int_\Omega \gamma_\beta(\beta)\, \mathrm{d}V, \tag{5}$$

where $S_\beta = \{\beta | \beta(\mathbf{x}) = 1, \forall \mathbf{x} \in \Gamma^I\}$ and γ_β is defined as

$$\gamma_\beta(\beta) = \frac{1}{2\ell_\beta}\beta^2 + \frac{\ell_\beta}{2}\nabla\beta \cdot \nabla\beta. \tag{6}$$

The regularized interface representation Γ_β from the above variation principle converges for $\ell_\beta \to 0$ to the exact sharp interface Γ^I. In the following, both length scale parameters ℓ_d and ℓ_β are assumed to be equal, i.e. $\ell_d = \ell_\beta = \ell$. Moreover, the interfaces are assumed to be fixed, i.e. $\beta(\mathbf{x})$ is kept unchanged during the simulation. The physical relevance of ℓ_β is analogous with ℓ_d and then ℓ_β loses its interpretation as crack interface width and can be seen as a supplementary material parameter. Identifying such parameters by inverse approaches as in [39] is beyond the scope of the present paper.

To construct $\beta(\mathbf{x})$, we first construct a level-set function $\psi(\mathbf{x})$ such that the interfaces define the zero-level-set of $\psi(\mathbf{x})$. In voxel-based images, this can

be achieved by defining interface nodes and constructing $\psi(\mathbf{x})$ as a signed distance to these nodes (see e.g. [42]). Then, nodes having an absolute value higher than a given threshold (0.8 in the present work) are associated to Dirichlet boundary conditions $\beta = 1$ to solve the problem (4) to obtain $\beta(\mathbf{x})$.

2.3 Regularized representation of the displacement jumps within interfaces

We define two types of displacement jump within the present context. The first one is due to the interface debounding and the other is due to bulk crack opening. We propose to evaluate both discontinuities through a regularized approximation as developed in [42].

In order to derive a unified description of the displacement jump $[\![\mathbf{u}(\mathbf{x})]\!]$ for both types of discontinuity, we first define the indicator function $\phi(\mathbf{x})$ from $d(\mathbf{x})$ and $\beta(\mathbf{x})$ (see Fig. 1) as:

$$\phi(\mathbf{x}) = \max\{d(\mathbf{x}), \beta(\mathbf{x})\}. \tag{7}$$

Using this definition, the displacement jump field $[\![\mathbf{u}(\mathbf{x})]\!]$ can be approximated using (see Fig. 2) [42]:

$$[\![\mathbf{u}(\mathbf{x})]\!] \approx \mathbf{u}(\mathbf{x}^+) - \mathbf{u}(\mathbf{x}^-) \tag{8}$$

where by using a Taylor expansion at first order

$$\mathbf{u}(\mathbf{x}^\pm) \approx \mathbf{u}(\mathbf{x}) \pm \frac{h}{2}\nabla\mathbf{u}(\mathbf{x}) \cdot \mathbf{n}^\phi, \tag{9}$$

and where h is a small expansion parameter. In the present work, it is chosen as the characteristic element size in the vicinity of the crack. The normal vector in (9) $\mathbf{n}^\phi$ can be determined using the indicator field $\phi(\mathbf{x})$ by:

$$\mathbf{n}^\phi = \frac{\nabla\phi(\mathbf{x})}{\|\nabla\phi(\mathbf{x})\|}. \tag{10}$$

It should be noted here that the above evaluation of the normal is different from the strategy applied in our previous work [42], where a level-set function was constructed for the evaluation of the interface normal. This is because in this work the displacement jump field needs to be evaluated not only on the fixed interface, but also on the evolving crack. Therefore, we follow [29] and compute the normal using directly the indicator function $\phi(\mathbf{x})$. The approximate displacement jump field is then expressed as:

$$[\![\mathbf{u}(\mathbf{x})]\!] \approx \mathbf{w}(\mathbf{x}) = h\nabla\mathbf{u}(\mathbf{x}) \cdot \mathbf{n}^\phi. \tag{11}$$

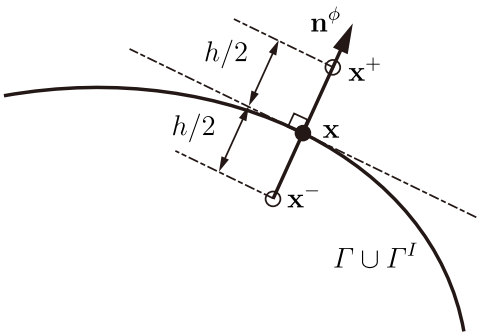

Fig. 2. Approximation of the displacement jump across the interface and the crack.

Here, h is a characteristic length parameter and $\mathbf{w}(\mathbf{x})$ denotes the regularized approximation of the displacement jump. It has been shown in our previous work [42] that the lowest estimation error is reached for $h = h^{\mathrm{e}}$, with h^{e} the typical element size of the finite element mesh. Note that in the current regularized framework, the diffuse displacement jump field $\mathbf{w}(\mathbf{x})$ is not only defined at the the cracks and interfaces, but over the whole domain Ω.

In the following, $\mathbf{w}$ will be used to define the additional Poiseuille-type fluid flow within the fracture and the cohesive interfacial effect, respectively, so as to propose a unified scheme to allow for fluid flow within both matrix cracks and interfacial cracks.

3 Phase field modeling of hydraulic fracturing and interfacial damage

In this section, we extend the phase field hydraulic fracturing framework developed recently by Miehe et al. [29] to heterogeneous media by accounting for interfacial damage [42]. The governing equations of fluid-saturated deformable porous medium according to the generalized Biot's theory are first reviewed in Section 3.1. Phase field modeling of poroelasticity is presented thereafter in Section 3.2. The thermodynamics for the evolution of the crack phase field is given in Section 3.3.

3.1 Governing equations of poroelasticity

The linear momentum balance equation for the porous medium saturated with fluid reads

$$\nabla \cdot \boldsymbol{\sigma} = \mathbf{0}, \tag{12}$$

where body forces have been neglected and where $\boldsymbol{\sigma}$ denotes the total stress decomposed as:

$$\boldsymbol{\sigma} = \boldsymbol{\sigma}_{\text{eff}} - bp\mathbf{1}, \tag{13}$$

where $\boldsymbol{\sigma}_{\text{eff}}$ is the Biot's effective stress, p is the pore fluid pressure and b is the Biot's effective stress coefficient given by

$$b = 1 - K_d/K_s, \tag{14}$$

where K_d i the drained bulk modulus of the porous medium and K_s is its unjacketed modulus, equivalent to the bulk modulus of its solid phase. The constitutive equation of the solid phase can be written as:

$$\boldsymbol{\sigma}_{\text{eff}} = \mathbb{D} : \nabla^s \mathbf{u}, \tag{15}$$

where

$$(\nabla^s \mathbf{u})_{ij} = (u_{i,j} + u_{j,i})/2 \tag{16}$$

is the linearized strain and $\mathbb{D}$ is the fourth-order elastic stiffness tensor of the solid skeleton. Throughout this paper, the stress is defined as tension positive, while the fluid pressure is defined as compression positive [36]. The continuity equation for the fluid flow can be written as:

$$\dot{\theta} + \nabla \cdot \mathbf{q} = 0, \tag{17}$$

where $\mathbf{q}$ is the fluid flux and θ is the fluid content, which is defined as the fluid volume per unit volume of porous material [5]:

$$\dot{\theta} = \frac{1}{M}\dot{p} + b\nabla \cdot \dot{\mathbf{u}}. \tag{18}$$

Here $\mathbf{u}$ is the displacement field of the solid skeleton and M is the Biot's modulus defined as

$$\frac{1}{M} = \frac{m}{K_f} + \frac{b-m}{K_s} \tag{19}$$

where m is the porosity of the medium. The fluid flow is related to the pressure according to the Darcy's law through:

$$\mathbf{q} = -\mathbf{k}\nabla p \tag{20}$$

in which $\mathbf{k}$ is the permeability tensor of the porous medium. In the case of a homogeneous isotropic porous medium, $\mathbf{k}$ can be replaced by $k_{\text{homo}}/\eta\mathbf{1}$, with k_{homo} the intrinsic permeability, η the dynamic viscosity of the fluid and $\mathbf{1}$ is the second-order identity tensor. Substituting the fluid concentration (18) and

the flow (20) into the fluid continuity equation (17) results into:

$$\frac{1}{M}\dot{p} + b\nabla \cdot \dot{\mathbf{u}} - \mathbf{k}\nabla^2 p = 0. \tag{21}$$

Eqs. (12) and (21) are completed with boundary conditions, defined as:

$$\begin{cases} \mathbf{u} = \bar{\mathbf{u}} \ \text{ on } \ \partial\Omega_u \\ \boldsymbol{\sigma} \cdot \mathbf{n} = \bar{\mathbf{t}} \ \text{ on } \ \partial\Omega_t \end{cases} \quad \text{and} \quad \begin{cases} p = \bar{p} \ \text{ on } \partial\Omega_p \\ \mathbf{q} \cdot \mathbf{n} = \bar{q} \ \text{ on } \partial\Omega_q, \end{cases} \tag{22}$$

where the prescribed displacements, pressure, traction and external fluid flux are denoted by $\bar{\mathbf{u}}$, $\bar{p}$, $\bar{\mathbf{t}}$ and $\bar{q}$, respectively. In the above, $\partial\Omega_t$ and $\partial\Omega_u$ denote Neumann and Dirichlet boundaries for the mechanical problem, respectively, and $\partial\Omega_q$ and $\partial\Omega_p$ denote Neumann and Dirichlet boundaries for the fluid problem, such that:

$$\begin{cases} \partial\Omega = \partial\Omega_t \cup \partial\Omega_u \ \text{ and } \ \partial\Omega_t \cap \partial\Omega_u = \emptyset \\ \partial\Omega = \partial\Omega_q \cup \partial\Omega_p \ \text{ and } \ \partial\Omega_q \cap \partial\Omega_p = \emptyset. \end{cases} \tag{23}$$

3.2 Phase field modeling of poroelasticity

The two main strong form equations for poroelasticity problem in the previous section are summarized as follows:

$$\begin{cases} \nabla \cdot \boldsymbol{\sigma} = \mathbf{0}, \ \text{ with } \ \boldsymbol{\sigma} = \boldsymbol{\sigma}_{\text{eff}} - bp\mathbf{1}, \\ \frac{1}{M}\dot{p} + b\nabla \cdot \dot{\mathbf{u}} - \mathbf{k}\nabla^2 p = 0, \end{cases} \tag{24}$$

together with the prescribed boundary conditions (22). In the following, we introduce the effects of both matrix and interfacial damage in the above equations.

3.2.1 Bulk contribution

Including crack and interface phase fields $d(\mathbf{x})$ and $\beta(\mathbf{x})$, the effective stress is modified according to:

$$\boldsymbol{\sigma}_{\text{eff}} = \Big((1-d)^2 + \kappa\Big)\,\boldsymbol{\sigma}^{+}_{\text{eff}} + \boldsymbol{\sigma}^{-}_{\text{eff}}, \tag{25}$$

where $\kappa \ll 1$ is a small positive parameter introduced to prevent the singularity of the stiffness matrix due to fully broken parts, $\boldsymbol{\sigma}^{+}_{\text{eff}}$ and $\boldsymbol{\sigma}^{-}_{\text{eff}}$ are the tensile and compressive stresses

$$\boldsymbol{\sigma}^{\pm}_{\text{eff}} = \lambda\langle \text{tr}[\tilde{\boldsymbol{\varepsilon}}]\rangle_{\pm}\mathbf{1} + 2\mu\tilde{\boldsymbol{\varepsilon}}^{\pm} \tag{26}$$

with λ and μ the Lamé coefficients of the porous matrix. Only tensile damage degradation is taken into account in the elastic energy (25) through a decomposition of the elastic strain $\tilde{\varepsilon}$ into tensile and compressive parts [32]:

$$\tilde{\boldsymbol{\varepsilon}} = \tilde{\boldsymbol{\varepsilon}}^{+} + \tilde{\boldsymbol{\varepsilon}}^{-} \quad \text{with} \quad \tilde{\boldsymbol{\varepsilon}}^{\pm} = \sum_{i=1}^{3} \langle \tilde{\varepsilon}^{i} \rangle_{\pm} \mathbf{n}^{i} \otimes \mathbf{n}^{i}. \tag{27}$$

In the above, $\langle x \rangle_{\pm} = (x \pm |x|)/2$, and $\tilde{\varepsilon}^{i}$ and $\mathbf{n}^{i}$ are the eigenvalues and eigenvectors of $\tilde{\boldsymbol{\varepsilon}}$. Note that in Eq. (25) an alternative notation $\tilde{\boldsymbol{\varepsilon}}$ is adopted for the strain rather than $\boldsymbol{\varepsilon}$. This is because within the continuously defined phase field framework, there exits no distinct separation between the bulk and the interface kinematics and thus the strain induced by the approximate displacement jump $\mathbf{w}$ needs to be substracted from the strain tensor [50,42]:

$$\tilde{\boldsymbol{\varepsilon}} = \nabla^{s}\mathbf{u} - \mathbf{n}^{\phi} \otimes^{s} \mathbf{w}\gamma_{\beta}, \tag{28}$$

where the second term represents the strain induced by the diffused displacement jump

$$(\mathbf{n}^{\phi} \otimes^{s} \mathbf{w})_{ij} = (n_i^{\phi} w_j + w_i n_j^{\phi})/2. \tag{29}$$

3.2.2 Cohesive interface modeling

Cohesive constitutive behavior is assumed at the smeared interface zone through a traction-separation law as:

$$\mathbf{t}(\mathbf{w}, \boldsymbol{\alpha}) = \frac{\partial \psi^{I}(\mathbf{w}, \boldsymbol{\alpha})}{\partial \mathbf{w}} \tag{30}$$

where ψ^{I} is the fracture energy function depending on the displacement jump $\mathbf{w}$ from (11) and $\boldsymbol{\alpha}$ is a vector of history parameters. It has been shown in our recent work [42] that history parameters $\boldsymbol{\alpha}$ can be omitted with negligible influence within the phase field fracturing framework as the irreversible crack phase field serves implicitly as history variable.

Even though the problem is not restricted to this case, we neglect in the following the effects of the tangential component in the cohesive model, which then simplifies to:

$$\mathbf{t}(w^{n}) = \frac{\partial \psi^{I}(w^{n})}{\partial \mathbf{w}} \tag{31}$$

in which w^{n} is the normal displacement jump along the interface defined as

$$w^{n} = \mathbf{w} \cdot \mathbf{n}^{\phi}, \tag{32}$$

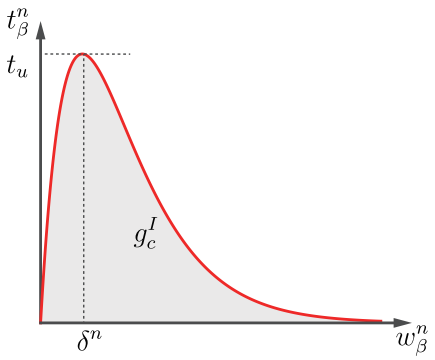

Fig. 3. Illustration of the traction-separation curve of the typical cohesive model in (33).

where the normal $\mathbf{n}^\phi$ and the approximate field $\mathbf{w}$ are given in (10) and (11). One conventional nonlinear elastic cohesive model without dependency on history can be expressed as [49]

$$t^n = \mathbf{t} \cdot \mathbf{n}^\phi = g_c^I \frac{w^n}{\delta^n} \exp(-\frac{w^n}{\delta^n}), \tag{33}$$

in which δ^n is related to the interface fracture toughness g_c^I and the interface fracture strength t_u through:

$$\delta^n = g_c^I/(t_u e) \tag{34}$$

where $e = \exp(1)$. This relationship is illustrated in Fig. 3, where the fracture toughness g_c^I denotes the value of the interface energy function ψ^I at full crack opening.

3.2.3 Anisotropic fluid flow modeling of the cracked porous medium

A Poiseuille-type fluid flow is assumed [29] within the cracks and the crack phase field $d(\mathbf{x}, t)$ is adopted to serve as an indicator for the evolving anisotropic permeability. The permeability tensor $\mathbf{k}$ in the second equation of (24) is split into two parts using the crack phase field as an indicator

$$\overline{\mathbf{k}} = \mathbf{k} + (d)^\epsilon \, \mathbf{k}_{\text{crack}} \tag{35}$$

where $\epsilon \geq 1$ is an additional material parameter used to localize the increased permeability along the fracture. The anisotropic permeability $\mathbf{k}_{\text{crack}}$ dependent on the crack opening is defined as:

$$\mathbf{k}_{\text{crack}} = \left(\frac{(w^n)^2}{12\eta} - k_{\text{homo}} \right) \left(\mathbf{1} - \mathbf{n}^\phi \otimes \mathbf{n}^\phi \right). \tag{36}$$

Note that when the interfaces are damaged, the value of $d(\mathbf{x})$ increases in the

nodes in the neighborhood of the interfaces (see [42]) and then the permeability is modified according to (35) also in the interfaces. Then, the fluid is allowed to pass both through bulk and interface cracks in the present scheme.

3.3 Phase field evolution

Considering the problem defined in section 3.1, the total energy of a medium embedding cracks and cohesive interfaces in a standard framework reads:

$$J(\boldsymbol{\varepsilon},\theta) = \int_{\Omega} W_{\text{bulk}}(\boldsymbol{\varepsilon},\theta)\ \mathrm{d}V + \int_{\Gamma^I} \psi^I(\llbracket \mathbf{u} \rrbracket)\ \mathrm{d}A + \int_{\Gamma} g_c\ \mathrm{d}A, \tag{37}$$

in which ψ^I is the strain energy density function depending on the displacement jump $\llbracket \mathbf{u} \rrbracket$ across the interface Γ^I (the history parameter $\boldsymbol{\alpha}$ has been omitted, see Section 3.2.2 or [42]) and g_c is the critical fracture energy density, also named as Griffith's critical energy release rate.

In the present regularized framework, we introduce the fields $d(\mathbf{x})$ and $\beta(\mathbf{x})$ for the representation of crack and interface and replace also the corresponding strong displacement jumps $\llbracket \mathbf{u} \rrbracket$ by the approximation $\mathbf{w}(\mathbf{x})$ given in (11). Then (37) is replaced by a *total* pseudo-energy defined in the form:

$$J(\boldsymbol{\varepsilon},\theta,\beta,\mathbf{w};d) = \int_{\Omega} W_{\text{bulk}}(\tilde{\boldsymbol{\varepsilon}},\theta;d)\ \mathrm{d}V + \int_{\Omega} \psi^I(\mathbf{w})\gamma_\beta\ \mathrm{d}V + \int_{\Omega} (1-\beta)^2 g_c \gamma_d\ \mathrm{d}V \tag{38}$$

where γ_β and γ_d are the surface densities defined in (6) and (3). The factor $(1-\beta)^2$ is introduced here following our original proposition in [42] to ensure that the constitutive behavior along the interfaces is dominated by the applied cohesive model. In (38), γ_β is used to activate the cohesive model damage only at the inclusions/matrix interfaces.

Using (38), the *total* pseudo-energy potential or free energy W can be identified as:

$$W(\boldsymbol{\varepsilon},\theta,\beta,\mathbf{w};d) = W_{\text{bulk}}(\tilde{\boldsymbol{\varepsilon}},\theta;d) + W_{\text{inter}}(\beta,\mathbf{w}) + W_{\text{frac}}(\beta,d) \tag{39}$$

with

$$W_{\text{inter}} = \psi^I(\mathbf{w})\gamma_\beta \quad \text{and} \quad W_{\text{frac}} = (1-\beta)^2 g_c \gamma_d \tag{40}$$

and the bulk contribution as

$$W_{\text{bulk}} = (1-d)^2 \psi^+_{\text{eff}}(\tilde{\boldsymbol{\varepsilon}}) + \psi^-_{\text{eff}}(\tilde{\boldsymbol{\varepsilon}}) + \psi_{\text{fluid}}(\tilde{\boldsymbol{\varepsilon}},\theta). \tag{41}$$

The bulk contribution W_{bulk} is composed of three parts including the tensile and compressive effective strain energy of the porous matrix,

$$\psi_{\text{eff}}^{\pm} = \lambda \langle \text{tr}[\tilde{\boldsymbol{\varepsilon}}] \rangle_{\pm}^2 / 2 + \mu \text{tr}[\tilde{\boldsymbol{\varepsilon}}^{\pm}]^2, \tag{42}$$

and the contribution related to the fluid

$$\psi_{\text{fluid}} = \frac{M}{2}(\text{tr}[\tilde{\boldsymbol{\varepsilon}}]^2 - 2\theta[\tilde{\boldsymbol{\varepsilon}}] + \theta^2), \tag{43}$$

where the degradation applies only to the tensile effective strain energy in line with the assumption in (25). The small parameter κ appearing in (25) is omitted here in (42) to simplify the notation.

The evolution of the damage variable $d(\mathbf{x}, t)$ can then be determined by the variational derivative of W. In a rate-independent setting with the consideration of the reduced Clausius-Duhem inequality, the evolution criterion is provided by the Kuhn-Tucker conditions [32,41]:

$$\dot{d} \geq 0; \quad -\delta_d W \leq 0; \quad \dot{d}[-\delta_d W] = 0 \tag{44}$$

yielding

$$-\delta_d W = 2(1-d)\psi_{\text{eff}}^{+} - (1-\beta)^2 g_c \delta_d \gamma_d + (1-d)^2 \delta_d \psi_{\text{eff}}^{+} + \delta_d \psi_{\text{eff}}^{-} = 0 \tag{45}$$

Note that as $\tilde{\boldsymbol{\varepsilon}}$ is a function of $d(\mathbf{x})$ through (28), (10), (7) then $\delta_d \psi_{\text{eff}}^{+}$ and $\delta_d \psi_{\text{eff}}^{-}$ are non-zero. For the sake of simplification and justified by the fact that we are using in the present work a staggered scheme where at each iteration the mechanical problem is solved considering a fixed phase field $d(\mathbf{x})$ (see section 4), we assume in the following that $\delta_d \psi_{\text{eff}}^{+} \approx 0$ and $\delta_d \psi_{\text{eff}}^{-} \approx 0$.

In the above, [32]:

$$\delta_d \gamma_d = d/\ell_d - \ell_d \delta d. \tag{46}$$

The damage evolution criterion can be then expressed in the following form [28]:

$$(1-\beta)^2 \frac{g_c}{\ell_d}[d - \ell_d^2 \nabla^2 d] = 2(1-d) \max_{t \in [0,T]} \left\{ \psi_{\text{eff}}^{+}(\mathbf{x}, t) \right\}. \tag{47}$$

The criterion (47) is a monotonously increasing function of the strain $\tilde{\boldsymbol{\varepsilon}}(\mathbf{x}, t)$ that induces unnecessary stress degradation even at low strain values. To avoid this issue, an energetic damage evolution criterion with threshold has been introduced in [29]

$$(1-\beta)^2 2\psi_c[d - \ell_d^2 \nabla^2 d] = 2(1-d) \max_{t \in [0,T]} \left\{ \langle \psi_{\text{eff}}^{+}(\mathbf{x}, t) - \psi_c \rangle_{+} \right\}, \tag{48}$$

in which ψ_c is a specific fracture energy density of the porous matrix, which can be further related to a critical fracture stress σ_c by:

$$\psi_c = \frac{1}{2E}\sigma_c^2 \tag{49}$$

where E is the Young's modulus (see more details in [29]). The above evolution criterion in (48) can be further stated as

$$(1-\beta)^2 2\psi_c[d - \ell_d^2\nabla^2 d] = 2(1-d)\mathcal{H}(\mathbf{x},t) \tag{50}$$

with the introduction of a strain energy history function [29]

$$\mathcal{H}(\mathbf{x},t) = \max_{t\in[0,T]}\left\{\langle\psi_{\text{eff}}^{+}(\mathbf{x},t) - \psi_c\rangle_+\right\}. \tag{51}$$

We have shown in [42] that the present phase field with interfacial damage allows defining interfacial damage history by an increase of the field $d(\mathbf{x})$ in the interfaces when the cohesive model is activated. In this context, the field $d(\mathbf{x})$ plays the role of internal variable for the cohesive model. As the permeability within cracks is increased according to (36), then the present scheme allows the fluid to flow within both matrix and interface cracks in a simple manner.

We note that another possibility would be to use meshed interfaces with classical cohesive zones for interfaces, which would avoid the use of the field β. However, we have constructed this framework such that it can be applied to voxel-based images of heterogeneous media in which interfaces are stair-like. In this context, regularizing the interfaces allows representing in a consistent manner all discontinuities, in the same fashion that what is done with the phase field cracks.

4 Discretization and numerical implementation

In this section, we present the weak forms and discretizations by FEM of the coupled displacement-pressure problem and the crack phase field problems presented in Section 4.1.

4.1 Weak forms of governing equations

Multiplying the governing equations given in (24) by kinematically admissible test functions for the displacement $\delta\mathbf{u}$ of the porous matrix and for the pressure δp, integrating the resulting expression over the domain Ω, and using the

divergence theorem together with the boundary conditions (22) yields the associated weak forms:

$$\begin{cases} \int_\Omega (\boldsymbol{\sigma}_{\text{eff}} - bp\mathbf{1}) : \tilde{\boldsymbol{\varepsilon}}(\delta\mathbf{u})\,\mathrm{d}V + \int_\Omega \gamma_\beta \mathbf{t}\cdot\mathbf{w}(\delta\mathbf{u})\,\mathrm{d}V = \int_{\partial\Omega_t} \bar{\mathbf{t}}\cdot\delta\mathbf{u}\,\mathrm{d}A \\ \int_\Omega \frac{1}{M}\dot{p}\delta p\,\mathrm{d}V + \int_\Omega b\nabla\cdot\dot{\mathbf{u}}\delta p\,\mathrm{d}V - \int_\Omega \nabla p\cdot\overline{\mathbf{k}}\cdot\nabla\delta p\,\mathrm{d}V = -\int_{\partial\Omega_q}\bar{q}\delta p\,\mathrm{d}A \end{cases} \tag{52}$$

in the absence of body forces.

The associated weak form for the crack phase field evolution (50) can be obtained in a similar manner with a kinematically admissible test function δd [41]:

$$\int_\Omega \left\{ \left(2\mathcal{H} + (1-\beta)^2 2\psi_c\right) d\delta d + (1-\beta)^2 2\psi_c \ell_d^2 \nabla d\cdot\nabla(\delta d)\right\}\,\mathrm{d}V = \int_\Omega 2\mathcal{H}\delta d\,\mathrm{d}V. \tag{53}$$

4.2 Linearization of the coupled poroelasticity problem

For a fixed crack phase field, there exists three sources of nonlinearity for the coupled poroelasticity problem (52): the strain tensor decomposition (70), the interface cohesive model (71) and the crack opening-dependent anisotropic permeability (36). The coupled nonlinear system can be solved by means of a Newton-Raphson (NR) iterative solution scheme. From (52) we set the residuals as:

$$\begin{cases} \mathcal{R}_{\mathbf{u}} = \int_\Omega (\boldsymbol{\sigma}_{\text{eff}} - bp\mathbf{1}) : \tilde{\boldsymbol{\varepsilon}}(\delta\mathbf{u})\,\mathrm{d}V + \int_\Omega \gamma_\beta \mathbf{t}\cdot\mathbf{w}(\delta\mathbf{u})\,\mathrm{d}V - \int_{\partial\Omega_t} \bar{\mathbf{t}}\cdot\delta\mathbf{u}\,\mathrm{d}A = \mathbf{0} \\ \mathcal{R}_p = \int_\Omega \frac{1}{M}\dot{p}\delta p\,\mathrm{d}V + \int_\Omega b\nabla\cdot\dot{\mathbf{u}}\delta p\,\mathrm{d}V - \int_\Omega \nabla p\cdot\overline{\mathbf{k}}\cdot\nabla\delta p\,\mathrm{d}V + \int_{\partial\Omega_q}\bar{q}\delta p\,\mathrm{d}A = \mathbf{0}. \end{cases} \tag{54}$$

In a standard NR iterative solution scheme, both displacement and pressure fields are updated for each loading increment by solving the associated tangent problem:

$$\begin{cases} D_{\Delta\mathbf{u}}\mathcal{R}_{\mathbf{u}}\left(\mathbf{u}^{(k)}, p^{(k)}, d^{(k)}\right) + D_{\Delta p}\mathcal{R}_{\mathbf{u}}\left(\mathbf{u}^{(k)}, p^{(k)}, d^{(k)}\right) = -\mathcal{R}_{\mathbf{u}}\left(\mathbf{u}^{(k)}, p^{(k)}, d^{(k)}\right) \\ D_{\Delta\mathbf{u}}\mathcal{R}_p\left(\mathbf{u}^{(k)}, p^{(k)}, d^{(k)}\right) + D_{\Delta p}\mathcal{R}_p\left(\mathbf{u}^{(k)}, p^{(k)}, d^{(k)}\right) = -\mathcal{R}_p\left(\mathbf{u}^{(k)}, p^{(k)}, d^{(k)}\right). \end{cases} \tag{55}$$

where $D_{\Delta\mathbf{v}}\mathcal{R}(\mathbf{u})$ denotes the Gâteaux derivative defined as

$$D_{\Delta\mathbf{u}}\mathcal{R}(\mathbf{v}) = \left[\frac{d}{d\alpha}\left\{\mathcal{R}(\mathbf{v}+\alpha\Delta\mathbf{u})\right\}\right]_{\alpha=0}. \tag{56}$$

Here, $\mathbf{u}^{(k)}$ and $p^{(k)}$ are the displacement and pressure fields known from the previous (k-th) NR iteration. The corrections on the displacement and pressure are obtained as

$$\mathbf{u}^{(k+1)} = \mathbf{u}^{(k)} + \Delta\mathbf{u} \qquad \text{and} \qquad p^{(k+1)} = p^{(k)} + \Delta p. \tag{57}$$

4.3 Finite element discretization

As discussed in [56], the well-known LBB stability issue (e.g., [10]) for coupled poromechanical problems only occurs for the undrained limit case. When dealing with large permeability and/or time steps, the use of the same polynomial degree for both displacement and pressure fields is practicable [29]. In this work, we adopt the same finite element discretization using quadrilateral bilinear elements for the approximation of all three fields $(\mathbf{u}, p, d)$. We can express the three finite element approximate fields $(\mathbf{u}^h, p^h, d^h)$ as:

$$\mathbf{u}^h(\mathbf{x}) = \mathbf{N}_u(\mathbf{x})\mathbf{d}_u,\ p^h(\mathbf{x}) = \mathbf{N}_p(\mathbf{x})\mathbf{d}_p,\ d^h(\mathbf{x}) = \mathbf{N}_d(\mathbf{x})\mathbf{d}_d \tag{58}$$

and their gradients as

$$\nabla\mathbf{u}^h(\mathbf{x}) = \mathbf{B}_u(\mathbf{x})\mathbf{d}_u,\ \nabla p^h(\mathbf{x}) = \mathbf{B}_p(\mathbf{x})\mathbf{d}_p,\ \nabla d^h(\mathbf{x}) = \mathbf{B}_d(\mathbf{x})\mathbf{d}_d \tag{59}$$

where $\mathbf{N}_u, \mathbf{N}_p$ and $\mathbf{N}_d$ and $\mathbf{B}_u, \mathbf{B}_p$ and $\mathbf{B}_{dt}$ denote matrices of shape functions, and shape functions derivatives, respectively. Here, $\mathbf{d}_u, \mathbf{d}_p, \mathbf{d}_d$ denote the vectors of the nodal values of the finite element mesh for displacement, pressure and crack phase fields, respectively.

The Voigt's notation is adopted for the representation of the strain and stress in vector forms, as:

$$[\boldsymbol{\varepsilon}] = \mathbf{B}_u\mathbf{d}_u = [\varepsilon_{11}, \varepsilon_{22}, \varepsilon_{33}, 2\varepsilon_{23}, 2\varepsilon_{13}, 2\varepsilon_{12}]^{\mathrm{T}}. \tag{60}$$

A modified spatial strain-displacement matrix $\tilde{\mathbf{B}}_u$ is introduced such that

$$[\tilde{\boldsymbol{\varepsilon}}] = \tilde{\mathbf{B}}_u\mathbf{d}_u \quad \text{with} \quad \tilde{\mathbf{B}}_u = \mathbf{B}_u - h\gamma_\beta\mathbf{M}_\phi\mathbf{B}_w \tag{61}$$

in which $\mathbf{M}_\phi$ is a matrix defined in 2D by [42]:

$$\mathbf{M}_\phi = \begin{bmatrix} (n_1^\phi)^2 & n_1^\phi n_2^\phi & 0 & 0 \\ 0 & 0 & n_1^\phi n_2^\phi & (n_2^\phi)^2 \\ n_1^\phi n_2^\phi & (n_1^\phi)^2 & (n_2^\phi)^2 & n_1^\phi n_2^\phi \end{bmatrix} = \begin{bmatrix} n_1^\phi & 0 \\ 0 & n_2^\phi \\ n_2^\phi & n_1^\phi \end{bmatrix} \mathbf{N}_\phi \tag{62}$$

and

$$\mathbf{N}_\phi = \begin{bmatrix} n_1^\phi & n_2^\phi & 0 & 0 \\ 0 & 0 & n_1^\phi & n_2^\phi \end{bmatrix} \tag{63}$$

and $\mathbf{B}_w$ is a matrix of the shape function derivatives for the evaluation of displacement gradient satisfying in the 2D case

$$\mathbf{B}_w \mathbf{d}_u = \left[\frac{\partial u_1}{\partial x_1}, \frac{\partial u_1}{\partial x_2}, \frac{\partial u_2}{\partial x_1}, \frac{\partial u_2}{\partial x_2} \right]^{\mathrm{T}}. \tag{64}$$

Then, the displacement jump approximation vector $\mathbf{d}_w$ can be expressed as:

$$\mathbf{d}_w = h \mathbf{N}_\phi \mathbf{B}_w \mathbf{d}_u. \tag{65}$$

Introducing the above discretization into the linearized system (55), we obtain the following coupled discrete system of equations:

$$\begin{bmatrix} \mathbf{0} & \mathbf{0} \\ \mathbf{K}_{up}^{\mathrm{T}} & \mathbf{K}_{pp}^{(1)} \end{bmatrix}^{(k)} \frac{\mathrm{d}}{\mathrm{d}t} \begin{Bmatrix} \Delta \mathbf{d}_u \\ \Delta \mathbf{d}_p \end{Bmatrix} + \begin{bmatrix} \mathbf{K}_{uu} & -\mathbf{K}_{up} \\ \mathbf{0} & \mathbf{K}_{pp}^{(2)} \end{bmatrix}^{(k)} \begin{Bmatrix} \Delta \mathbf{d}_u \\ \Delta \mathbf{d}_p \end{Bmatrix} = \begin{Bmatrix} -\mathbf{R}_{\mathbf{u}} \\ -\mathbf{R}_p \end{Bmatrix}^{(k)}, \tag{66}$$

where the tangent stiffness matrices at the current $k-th$ NR iteration are defined by:

$$\begin{aligned} &\mathbf{K}_{uu} = \mathbf{K}_{\text{solid}} + \mathbf{K}_{\text{inter}}, && \mathbf{K}_{up} = \textstyle\int_\Omega b \tilde{\mathbf{B}}_u^{\mathrm{T}} [\mathbf{1}] \mathbf{N}_p \, \mathrm{d}V, \\ &\mathbf{K}_{pp}^{(1)} = \textstyle\int_\Omega M^{-1} \mathbf{N}_p^{\mathrm{T}} \mathbf{N}_p \, \mathrm{d}V, && \mathbf{K}_{pp}^{(2)} = \textstyle\int_\Omega \mathbf{B}_p^{\mathrm{T}} [\overline{\mathbf{k}}] \mathbf{B}_p \, \mathrm{d}V. \end{aligned} \tag{67}$$

The right-hand terms of (66) are the residuals at the current NR iteration

$$\begin{cases} \mathbf{R}_{\mathbf{u}}^{(k)} = \mathbf{K}_{uu}^{(k)} \mathbf{d}_u^{(k)} - \mathbf{K}_{up}^{(k)} \mathbf{d}_p^{(k)} - \int_{\partial\Omega_t} \mathbf{N}_u^{\mathrm{T}} \bar{\mathbf{t}} \, \mathrm{d}A \\ \mathbf{R}_p^{(k)} = (\mathbf{K}_{up}^{\mathrm{T}})^{(k)} \frac{\mathrm{d}}{\mathrm{d}t} \mathbf{d}_u^{(k)} + (\mathbf{K}_{pp}^{(1)})^{(k)} \frac{\mathrm{d}}{\mathrm{d}t} \mathbf{d}_p^{(k)} + (\mathbf{K}_{pp}^{(2)})^{(k)} \mathbf{d}_p^{(k)} + \int_{\partial\Omega_q} \mathbf{N}_p^{\mathrm{T}} \bar{q} \, \mathrm{d}A. \end{cases} \tag{68}$$

Above, $\mathbf{K}_{uu}$ is the stiffness matrix related to the displacement field, composed of the contribution due to the skeleton $\mathbf{K}_{\text{solid}}$ and due to the cohesive interfaces $\mathbf{K}_{\text{inter}}$. The matrix $\mathbf{K}_{up}$ is a coupling matrix and $\mathbf{K}_{pp}^{(2)}$ is associated with the pressure. The solid skeleton matrix $\mathbf{K}_{\text{solid}}$ is defined as:

$$\mathbf{K}_{\text{solid}} = \int_\Omega \tilde{\mathbf{B}}_u^{\mathrm{T}} \mathbf{D}_{\text{solid}} \tilde{\mathbf{B}}_u \, \mathrm{d}V, \tag{69}$$

where $\mathbf{D}_{\text{solid}}$ is the constitutive matrix corresponding to the definition in (25), given by:

$$\mathbf{D}_{\text{solid}} = \frac{\partial [\boldsymbol{\sigma}_{\text{eff}}]}{\partial [\tilde{\boldsymbol{\varepsilon}}]} = (1-d)^2 \left(\lambda \mathcal{R}^+ [\mathbf{1}][\mathbf{1}]^{\mathrm{T}} + 2\mu \mathbf{P}^+ \right) + \left(\lambda \mathcal{R}^- [\mathbf{1}][\mathbf{1}]^{\mathrm{T}} + 2\mu \mathbf{P}^- \right), \tag{70}$$

where $\mathcal{R}^\pm$ and $\mathbf{P}^\pm$ are two operators for the decomposition of strain into the tensile and compressive parts (see e.g., [41]). It is worth noting that the operators $\mathbf{P}^\pm$ are constructed by using the same vector notation than the

strain vector. The cohesive interface matrix $\mathbf{K}_{\text{inter}}$ is defined by:

$$\mathbf{K}_{\text{inter}} = \int_{\Omega} h^2 \gamma_\beta \mathbf{B}_w^{\mathrm{T}} \mathbf{N}_\phi^{\mathrm{T}} \mathbf{D}_{\text{inter}} \mathbf{N}_\phi \mathbf{B}_w \, \mathrm{d}V, \tag{71}$$

where $\mathbf{D}_{\text{inter}} = \partial \mathbf{t}_\beta / \partial \mathbf{w}_\beta$ is the constitutive matrix depending on the applied cohesive model.

To obtain a symmetric matrix system associated with equations in (66), we follow [55] and differentiate the first line in the equations of (66) with respect to time:

$$\begin{cases} \mathbf{K}_{uu} \frac{\mathrm{d}}{\mathrm{d}t} \Delta \mathbf{d}_u - \mathbf{K}_{up} \frac{\mathrm{d}}{\mathrm{d}t} \Delta \mathbf{d}_p = -\frac{\mathrm{d}}{\mathrm{d}t} \mathbf{R}_{\mathbf{u}} \\ \mathbf{K}_{up}^{\mathrm{T}} \frac{\mathrm{d}}{\mathrm{d}t} \Delta \mathbf{d}_u + \mathbf{K}_{pp}^{(1)} \frac{\mathrm{d}}{\mathrm{d}t} \Delta \mathbf{d}_p + \mathbf{K}_{pp}^{(2)} \Delta \mathbf{d}_p = -\mathbf{R}_p. \end{cases} \tag{72}$$

By reversing the signs of the first equation above, a symmetric matrix system is obtained as:

$$\begin{bmatrix} -\mathbf{K}_{uu} & \mathbf{K}_{up} \\ \mathbf{K}_{up}^{\mathrm{T}} & \mathbf{K}_{pp}^{(1)} \end{bmatrix}^{(k)} \frac{\mathrm{d}}{\mathrm{d}t} \begin{Bmatrix} \Delta \mathbf{d}_u \\ \Delta \mathbf{d}_p \end{Bmatrix} + \begin{bmatrix} \mathbf{0} & \mathbf{0} \\ \mathbf{0} & \mathbf{K}_{pp}^{(2)} \end{bmatrix}^{(k)} \begin{Bmatrix} \Delta \mathbf{d}_u \\ \Delta \mathbf{d}_p \end{Bmatrix} = \begin{Bmatrix} \frac{\mathrm{d}}{\mathrm{d}t} \mathbf{R}_{\mathbf{u}} \\ -\mathbf{R}_p \end{Bmatrix}^{(k)}. \tag{73}$$

We adopt the backward Euler finite difference scheme for the integration:

$$\left(\frac{\mathrm{d}(.)}{\mathrm{d}t} \right)^{t^{n+1}} \simeq \frac{(.)^{n+1} - (.)^n}{\Delta t}, \tag{74}$$

where Δt is the time increment and where $(.)^n$ and $(.)^{n+1}$ denote the unknowns at times t^n and t^{n+1}. Substituting (74) into (73) finally yields:

$$\begin{bmatrix} -\mathbf{K}_{uu} & \mathbf{K}_{up} \\ \mathbf{K}_{up}^{\mathrm{T}} & \mathbf{K}_{pp}^{(1)} + \Delta t \mathbf{K}_{pp}^{(2)} \end{bmatrix}^{(k)} \begin{Bmatrix} \Delta \mathbf{d}_u^{n+1} \\ \Delta \mathbf{d}_p^{n+1} \end{Bmatrix} = \begin{Bmatrix} \Delta \mathbf{R}_u \\ -\Delta t \mathbf{R}_p \end{Bmatrix}^{(k)} + \begin{bmatrix} -\mathbf{K}_{uu} & \mathbf{K}_{up} \\ \mathbf{K}_{up}^{\mathrm{T}} & \mathbf{K}_{pp}^{(1)} \end{bmatrix}^{(k)} \begin{Bmatrix} \Delta \mathbf{d}_u^n \\ \Delta \mathbf{d}_p^n \end{Bmatrix}. \tag{75}$$

The discretization of the phase field problem (53) leads to the following discrete system of equations:

$$\mathbf{K}_d \mathbf{d}_d = \mathbf{f}_d \tag{76}$$

where

$$\mathbf{K}_d = \int_{\Omega} \left\{ \left(2\mathcal{H} + (1-\beta)^2 2\psi_c \right) \mathbf{N}_d^{\mathrm{T}} \mathbf{N}_d + (1-\beta)^2 2\psi_c \ell_d^2 \mathbf{B}_d^{\mathrm{T}} \mathbf{B}_d \right\} \mathrm{d}V \tag{77}$$

and

$$\mathbf{f}_d = \int_{\Omega} 2\mathbf{N}_d^{\mathrm{T}} \mathcal{H} \, \mathrm{d}V. \tag{78}$$

In the above, $\mathcal{H}$ is strain energy history function defined in (51).

4.4 Overall algorithm

In the present work, a staggered scheme is employed following [29], where at each time increment the phase field problem is solved for fixed displacements and pressure known from the previous time step t^n. The mechanical problem is then solved given the phase field at the new time step t^{n+1}. The overall algorithm is described as follows.

(1) Set the initial fields $d(t_0), \mathbf{u}(t_0), p(t_0), \mathcal{H}(t_0)$ at time t_0.
(2) Compute $\beta(\mathbf{x})$ by solving (4).
(3) **Loop** over all time increments: at each time t^{n+1}:
  (a) Given $d(t^n), \mathbf{u}(t^n), p(t^n), \mathcal{H}(t^n)$:
  (b) Compute the history function $\mathcal{H}(t^{n+1})$ according to (51).
  (c) Compute the crack phase field $d(t^{n+1})$ by solving (76).
  (d) Approximate the displacement jump field $\mathbf{w}$ according to (11).
  (e) Compute $\mathbf{u}(t^{n+1})$ and $p(t^{n+1})$ with the current crack $d(t^{n+1})$ by solving (75).
  (f) $(.)^n \leftarrow (.)^{n+1}$ and go to (a).
(4) **End**.

5 Numerical examples

In this section, we first validate the performance of the phase field hydraulic fracturing by means of a series of benchmark tests and then apply the technique to hydraulic fracture in highly heterogeneous materials with possible interfacial damage. More critical studies on how the crack opening is computed and analytical solutions for fluid flow within the crack can be found in [30,29].

In all 2D examples, uniform meshes of quadrilateral bilinear elements with the plane strain assumption have been employed. The same finite element discretization has been chosen for all three fields $(\mathbf{u}, p, d)$. The characteristic length parameter for the displacement jump approximation appearing in (11) is set to be equal to the typical finite element size $h = h^e$, which gives the lowest estimation error as shown in [42]. The permeability transition exponent appearing in (35) is set to $\epsilon = 50$ following [30,29] such that the additional fluid flow can be localized within the crack.

The material properties of the homogeneous porous medium or constituting

the matrix in the following examples are given in Table 1. Note that when ISO units are used, the elasticity constants are of the order of 10^9 Pa, whereas the Biot effective stress coefficient is between 0 and 1 and the coefficient $1/M$ is about of the order of about 10^{-9} Pa^{-1}, resulting into ill-conditioning of the global matrix. To avoid this issue, we adopt GPa unit for pressure and elasticity constants, and 10^9 kg for mass as suggested in [55,43].

5.1 Hydraulic fracturing of homogeneous porous medium

A rectangular domain of dimensions 80×40 m^2 is considered as illustrated in Fig. 4. All displacements are fixed in both directions over the external boundary and the fluid pressure along the external boundary is set to zero. A constant flow of 0.003 m^2/s is injected into an initially defined crack of length 8 m at the center of the domain. The pre-existing crack is simulated by prescribing Dirichlet conditions on the crack phase field with $d = 1$ along the crack. The material properties of the homogeneous porous medium are listed in Table 1. The fluid injection lasts for $T = 24$ s and a constant time increment step $\Delta t = 0.1$ s has been chosen for the simulation. The characteristic length scale parameter for the crack phase field approximation is set to $l_d = 0.75$ m. The domain is uniformly discretized into 320×160 quadrilateral finite elements. Fig. 5 shows the evolutions of the crack phase field, the vertical displacement field and the fluid pressure field at three different times. As can be observed from Fig. 5(a), the initially defined crack propagates horizontally towards the two side boundaries. The displacement and fluid pressure plots as shown in Fig. 5(b) and (c) are in good agreement with the results provided in [36] using the extended finite element method. We observe that the fluid

Table 1
Material properties of the homogeneous porous medium [36].

Name	Symbol	Value	Unit
Young's modulus	E	15.96	GPa
Poisson's ratio	ν	0.2	[-]
Biot's effective stress coefficient	b	0.79	[-]
Biot's modulus	M	12.5	GPa
Intrinsic permeability (5.1,5.2,5.4)	k_{homo}	2×10^{-14}	m^2
Intrinsic permeability (5.3,5.5)	k_{homo}	2×10^{-20}	m^2
Fluid dynamic viscosity	η	1×10^{-3}	kg/(m·s)
Critical effective stress	σ_c	0.45	MPa

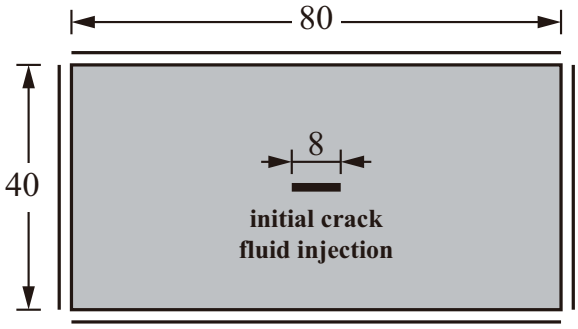

Fig. 4. Homogeneous porous medium subject to a constant fluid injection through an initial crack. External boundaries are mechanically restrained and are assumed to be permeable.

pressure is nearly constant within the crack due to the increased permeability along the main direction of the crack. Because the chosen time step is small as compared with the characteristic fluid diffusion, the fluid pressure outside the crack is much lower than the pressure within the regularized crack.

Fig. 6 shows the maximum fluid pressure within the crack versus the fluid injection time. As can be observed, the fluid pressure increases within the crack before reaching a peak point where the initially defined crack begins to propagate, resulting into a drop of the fluid pressure. This observation of the fluid drop is a well-known phenomenon in hydraulic fracturing and has been reported in many other works [11,33,29,26]. The same simulation has been repeated on two other finite element mesh of resolutions 160×80 and 640×320 elements to study the convergence with respect to the mesh size. Results are provided in Fig. 6, demonstrating the convergence of the method. In the following, a mesh of 160×80 elements has been used to limit the computational costs.

In the following, we investigate the influence of the intrinsic permeability of the homogeneous porous matrix on the hydraulic fracturing processing. The same problem as described above is used. Fig. 7 shows the influence of the intrinsic permeability on the pressure-time curve. As can be observed, when the intrinsic permeability takes a value lower than the permeability given in Table 1 (5×10^{-15} m^2), the reduced fluid diffusion outward the crack leads to a higher fluid pressure within the regularized crack before the cracking occurs. Fig. 8 provides the crack phase fields and the fluid pressure fields of the three mentioned cases at $t = 16$ s. It can be observed by comparing Fig. 8(a) and (b) that the lower the intrinsic permeability, the faster the crack propagates. This also explains the second sudden drop of the curve in the case $k_{\text{homo}} = 5 \times 10^{-15}$ m^2 in Fig. 7. At $t = 16$ s, the crack has already reached the two boundary ends and since then the fluid flows freely outward .

The adopted staggered scheme, following [29], requires small load time incre-

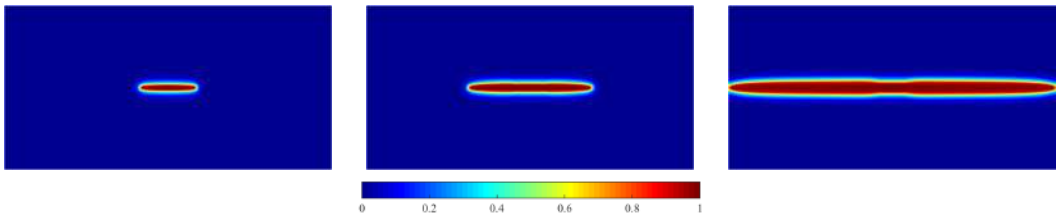

(a) Crack phase fields from left to right at $t = 2$ s, $t = 6$ s, $t = 24$ s.

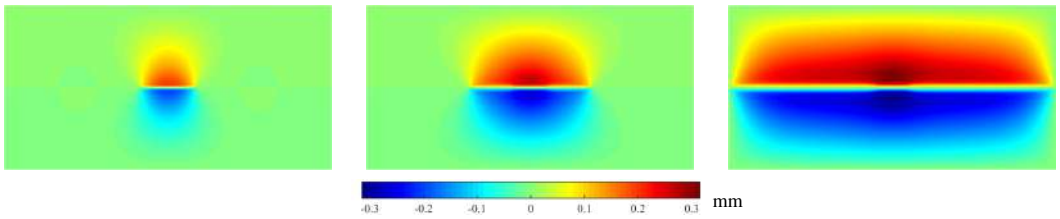

(b) Vertical displacement fields from left to right at $t = 2$ s, $t = 6$ s, $t = 24$ s.

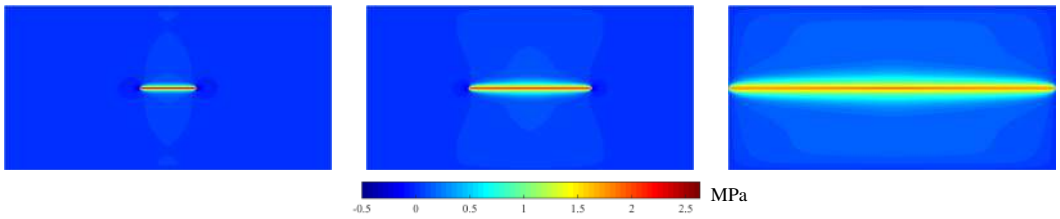

(c) Fluid pressure fields from left to right at $t = 2$s, $t = 6$s, $t = 24$s.

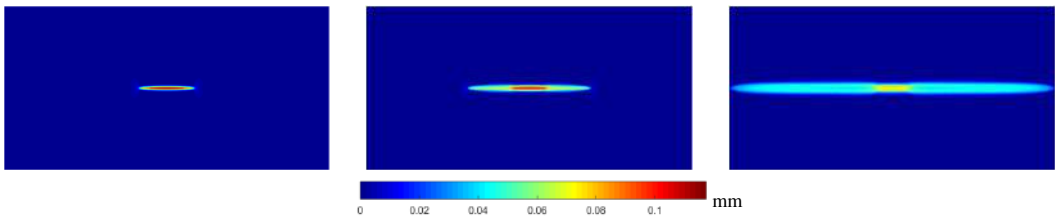

(d) Approximated displacement jump $w(\mathbf{x})$ at $t = 2$s, $t = 6$s, $t = 24$s.

Fig. 5. Evolution of crack phase, displacement and fluid pressure fields during the hydraulic fracturing of the homogeneous porous medium driven by a constant fluid injection.

ments. In the following, we investigate the influence of time increments by repeating the above simulation for $\Delta t = 0.05$ s and $\Delta t = 0.2$ s. Fig. 9 shows the curves of the maximum fluid pressure within the crack versus the fluid injection time for three different load time increments. From Fig. 9, the curve converges as the load time increment decreases. In the following tests, the load time increment has been set to $\Delta t = 0.1$ s to provide a good balance between simulation accuracy and computing costs.

We observe from Fig. 5 that away from the transition zone ($0 < d < 1$), there exists a damage plateau (with values $d \approx 1$) resulting into a "thick" crack. This is a common phenomenon for phase field hydraulic fracturing simulation as also observed in [33,29,26]. The formation of the plateau is due to the interaction between the fluid pressure contribution, which mainly depends on

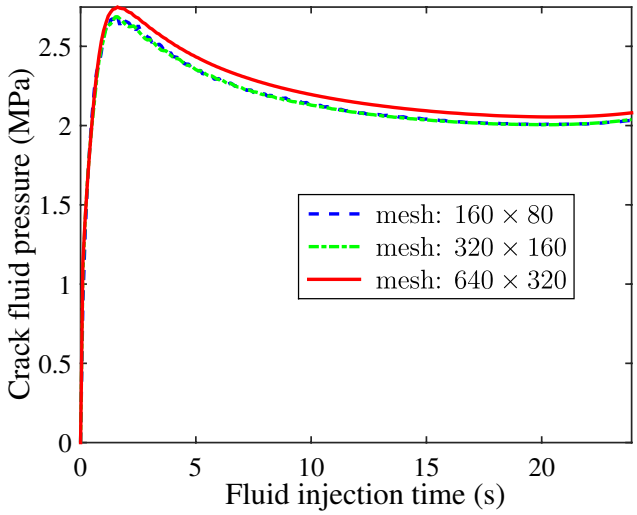

Fig. 6. Fluid pressure within the crack versus injection time for different mesh resolutions.

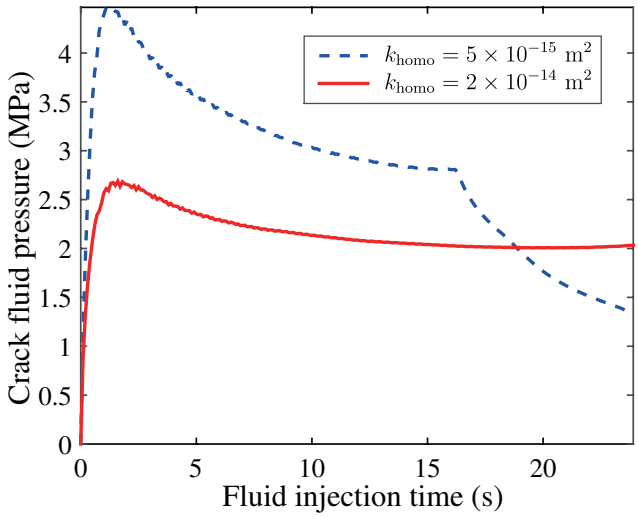

Fig. 7. Fluid pressure within the crack versus injection time for two different permeabilities of the porous medium.

the permeability of the surrounding porous medium. To our best knowledge, this issue is still an open question. We also note a "bone shape" of the crack in Fig. 5. We don't have a satisfactory explanation to this observation. The location of the slightly concave phase field distribution is where the Dirichlet boundary conditions of the phase field $d(\mathbf{x}) = 1$ is prescribed for the initial crack and where the fluid flux is imposed. Due to the prescribed boundary conditions (together with the fixed exterior displacements), the slightly concave region occurs where the largest displacement gradient takes place. Similar observations have also been reported in other works, e.g. in [29].

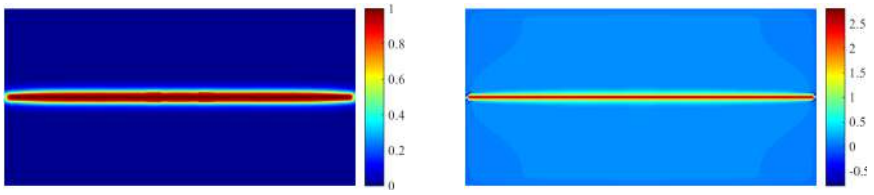

(a) Crack phase field and fluid pressure field with $k_{\text{homo}} = 5 \times 10^{-15}$ m^2 at $t = 16$ s.

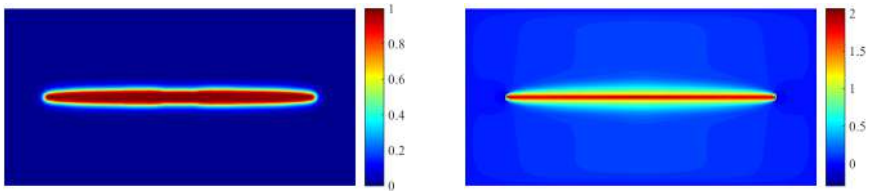

(b) Crack phase field and fluid pressure field with $k_{\text{homo}} = 2 \times 10^{-14}$ m^2 at $t = 16$ s.

Fig. 8. Comparison of the crack phase fields and the fluid pressure fields for two different intrinsic permeabilities of the homogeneous porous medium at $t = 16$ s.

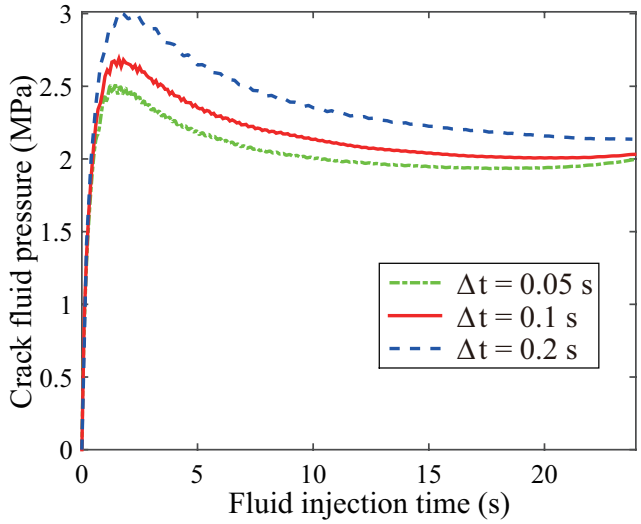

Fig. 9. Fluid pressure within the crack versus injection time for different load time increments.

5.2 Hydraulic fracturing of a heterogeneous medium with interfacial damage

A heterogeneous medium made of two material phases as shown in Fig. 10 is considered in this example. To define the microstructure, ellipsoidal inclusions are discretized within a regular 160×80 finite element mesh. The matrix is assumed to be a porous material whose parameters are provided in Table 1. The inclusions are supposed to be nearly impermeable by assigning a much lower intrinsic permeability value (1×10^{-19} m^2) as compared to the matrix and zero for the Biot's effective stress coefficient ($b = 0$). The inclusions are assumed to be much stiffer than the matrix with Young's modulus $E = 52$

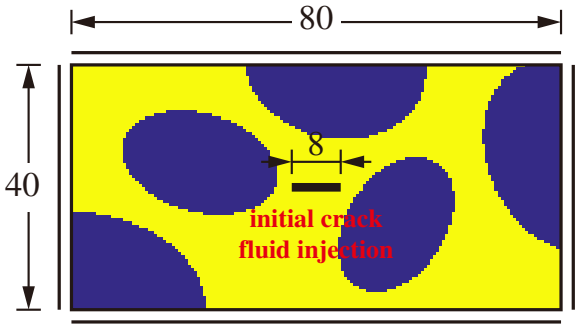

Fig. 10. A heterogeneous medium with ellipsoidal inclusions subjected to a constant fluid injection on an initial crack. All edges are mechanically restrained and are assumed to be permeable.

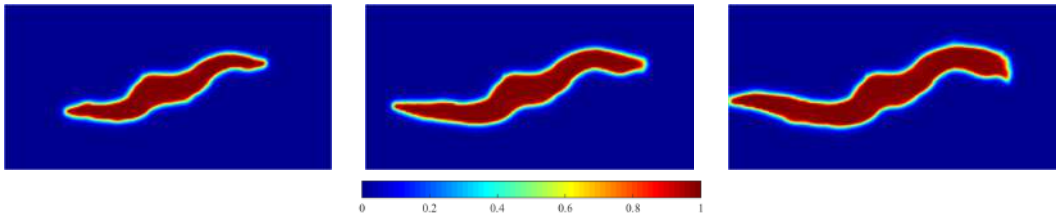

(a) Crack phase fields from left to right at $t = 24$ s, $t = 36$ s, $t = 48$ s.

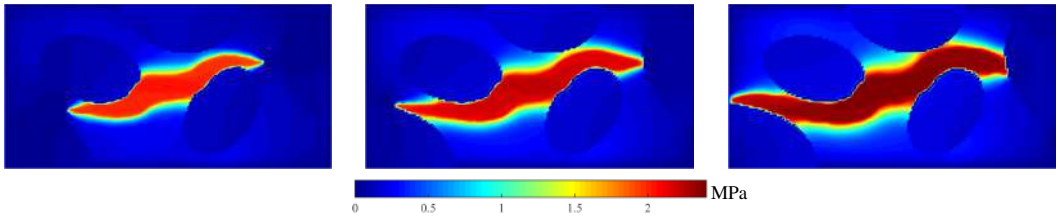

(b) Fluid pressure fields from left to right at $t = 24$ s, $t = 36$ s, $t = 48$ s.

Fig. 11. Evolution of the crack phase and fluid pressure during the hydraulic fracturing of the heterogeneous medium without considering the cohesive interfacial effect.

GPa and Poisson's ratio 0.2. The critical effective stress σ_c defined in (49) is assumed to be the same for the inclusions and for the matrix. All other parameters are the same as defined in the previous example.

A constant fluid flow as in the previous example is injected for 48 s. To evaluate the effects of the interfacial damage introduced in this work, we have conducted two simulations, one taking into account the interfacial damage and one neglecting it. Unlike the previous test, a much more complex crack path is observed due to the presence of the heterogeneities. As can be observed from the third plot in Fig. 11(b), the fluid pressure within the crack increases due to the arrest of the crack propagation towards the right edge.

An illustration of the construction of the level-set $\phi(\mathbf{x})$ and the associated function $\beta(\mathbf{x})$ for the present microstructure is depicted in Fig. 12. The characteristic length scale parameter for the interface phase field approximation is

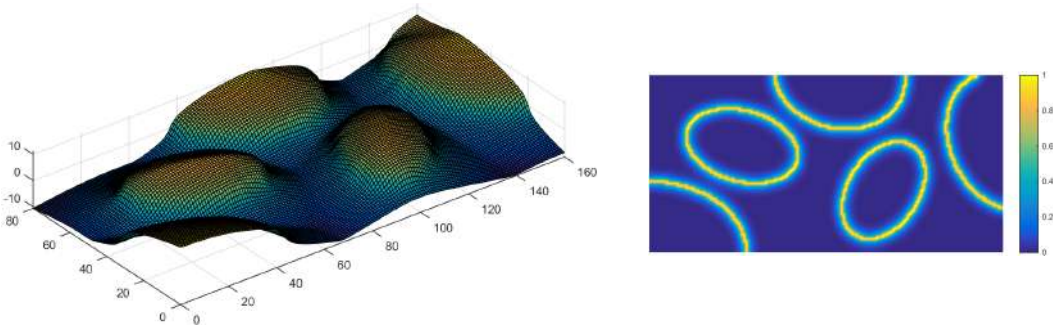

Fig. 12. Interface phase field determination: (a) level-set function $\psi(\mathbf{x})$ constructed as a signed distance function of the heterogeneous medium in Fig. 10, (b) the correspondingly determined interface phase field $\beta(\mathbf{x})$.

set equal to that of the crack phase field $\ell_\beta = \ell_d = 0.75$ m. We note that this technique is well-adapted for pixel-based images of realistic microstructures.

The simple cohesive model given in (33), taking into account damage only along normal traction, is adpoted. Two sets of parameters for the cohesive model, as illustrated in Fig. 13, are considered to illustrate the influence of the interfacial effect on crack propagation. For the first cohesive model, called "model I": $g_c^I = 7.5$ N/m and $t_u = 0.02$ MPa. For the second model, called "model II", $g_c^I = 10$ N/m and $t_u = 0.05$ MPa, inducing a higher strength than model I. Results for model I are presented in Fig. 14. As expected, the crack propagates around the two firstly encountered inclusions and the fluid pressure within the crack increases once the closed circulation is established until the end. Model II induces a different crack pattern, as shown in Fig. 15. Due to the higher traction force required to damage the interfaces, the crack that appears along the inclusion interface in the first case now merges with other neighboring interfacial cracks. Unlike the evolution of fluid pressure field in Fig. 14, the fluid pressure within the crack decreases (see Fig. 15) when the crack reaches the domain edges and when the fluid flows freely due to the zero pressure conditions. There is an interaction between the interfacial damage and the heterogeneities, as the heterogeneities create stress concentration in their vicinity, which interact with the interfacial damage. On the other hand, the parameter h affects the solution accuracy if not taken small enough.

5.3 Hydraulic fracturing of a realistic heterogeneous medium obtained from microtomography

In this example, we investigate the capabilities of the method to simulate hydro-mechanical cracks in realistic microstructures such as obtained by experimental imaging techniques, like X-ray microtomography for small dimensions of heterogeneities and techniques for geological heterogeneities at larger scales. The geometry is constructed by projecting a voxel-based image of a real

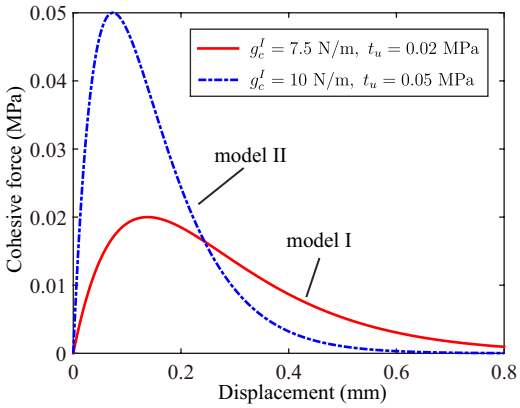

Fig. 13. Two cohesive models for analyzing the effects of the interfacial damage model.

.

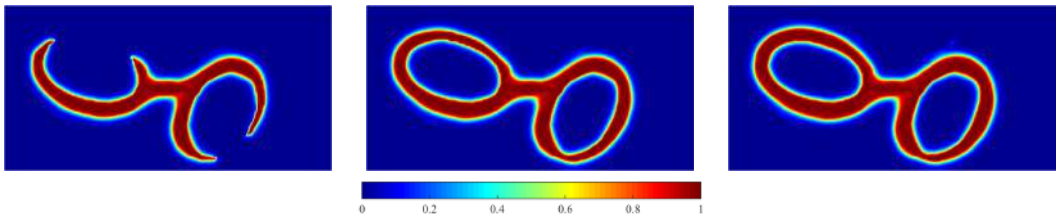

(a) Crack phase fields from left to right at $t = 24$ s, $t = 36$ s, $t = 48$ s.

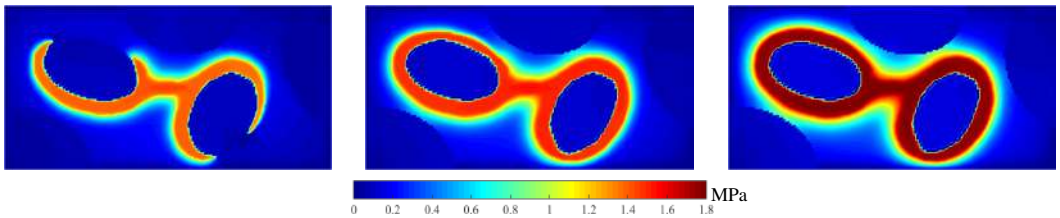

(b) Fluid pressure fields from left to right at $t = 24$ s, $t = 36$ s, $t = 48$ s.

Fig. 14. (a) Evolution of the crack phase field and (b) fluid pressure during the hydraulic fracturing of the heterogeneous medium considering the interfacial cohesive model I.

cementitious material obtained in [42] on a regular finite element mesh. The 2D segmented image consists in a single slice extracted from the 3D model. The image resolution is 480×480 and is depicted in Fig. 16(a). The dimensions of the domain is 48×48 mm^2. The properties of the matrix and inclusions are the same as in the previous example. For interfaces, the cohesive model II of the previous example has been used. The mesh matches the pixels of the original image and thus consists in 480×480 quadrilateral bilinear elements. As in the previous examples, the displacements and pressure are set to zero over the external boundary. A constant fluid flow of 0.003 mm^2/s is injected on a initial crack of length 4.8 mm during 48 s with a constant time step $\Delta t = 0.1$ s. The characteristic length scale parameters for both the crack phase field and the interface phase field are set to $\ell_d = \ell_\beta = 0.2$ mm.

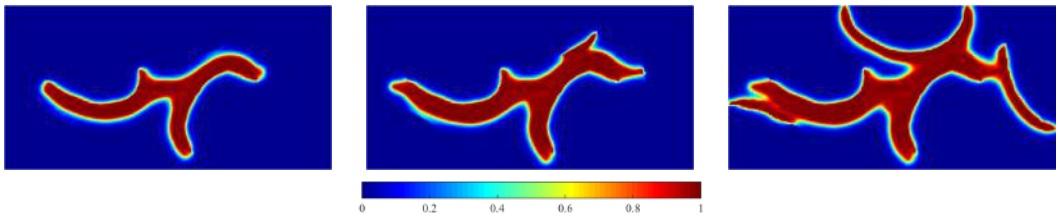

(a) Crack phase fields from left to right at $t = 24$ s, $t = 36$ s, $t = 48$ s.

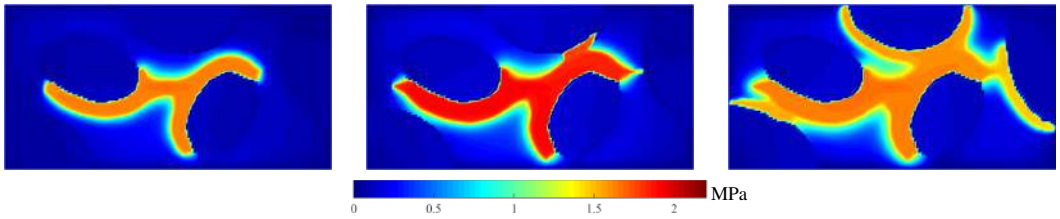

(b) Fluid pressure fields from left to right at $t = 24$ s, $t = 36$ s, $t = 48$ s.

Fig. 15. (a) Evolution of crack phase field and (b) fluid pressure during the hydraulic fracturing of the heterogeneous medium considering the interfacial cohesive model II.

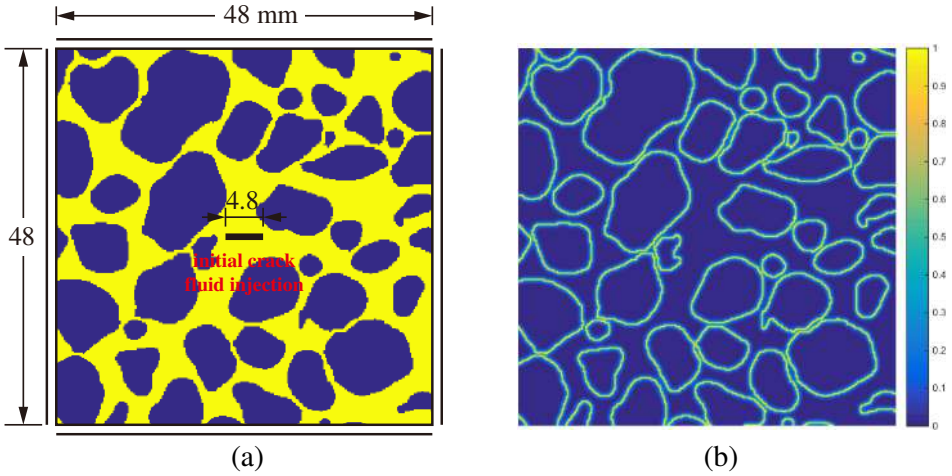

Fig. 16. Highly heterogeneous medium whose microtructure has been obtained by microtomography: (a) segmented image (b) corresponding interface phase field.

The function $\beta(\mathbf{x})$ for the geometry of the microstructure depicted in Fig. 16 (a) is provided in Fig. 16 (b). The evolution of both the crack phase field and the fluid pressure during the hydraulic fracturing test are depicted in Fig. 17. As expected, the crack propagates preferably along the interfaces. A very complex crack pattern results from the hydraulic fracturing simulation due to highly heterogeneous nature of the medium, and both crack branching and joining can be observed from Fig. 17(a). We further note from Fig. 17(b) that higher fluid pressure takes place around the injection position whereas the fluid pressure decreases gradually towards the domain edges with the crack propagation.

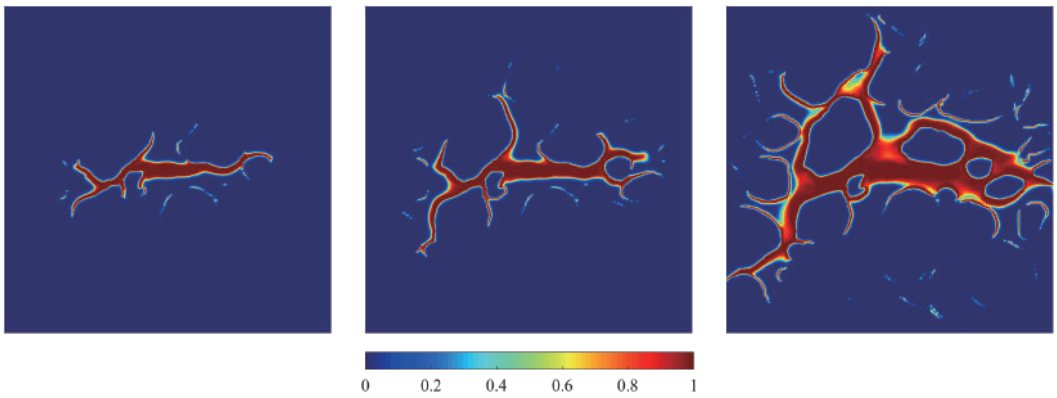

(a) Crack phase fields from left to right at $t = 6$ s, $t = 12$ s, $t = 48$ s.

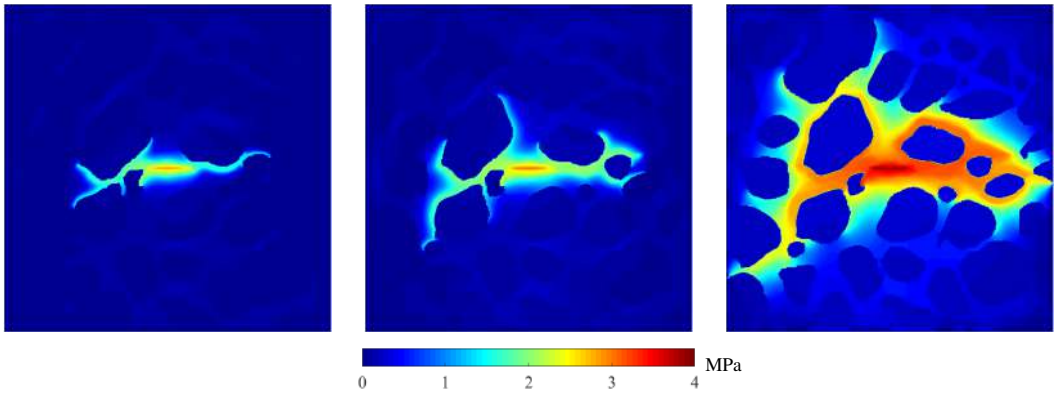

(b) Fluid pressure fields from left to right at $t = 6$ s, $t = 12$ s, $t = 48$ s.

Fig. 17. (a) Evolution of crack phase and (b) pressure during the hydraulic fracturing of the realistic heterogeneous medium considering the interfacial cohesive model II.

5.4 Hydraulic fracturing of a 3D homogeneous medium

In this example, we consider a 3D homogeneous medium made of the same porous material with properties given in Table 1 with an initial crack notch as shown in Fig. 18. The dimensions of the cubic domain are $80 \times 80 \times 40$ m^3. A constant fluid flow of 0.3 m^3/s is injected in an initial crack notch of surface 16×16 m^2 located at the center of the domain during 10 s with a constant time step $\Delta t = 0.1$ s. For the simulation, the cubic domain is discretized into $80 \times 80 \times 40$ eight-node cubic elements. The characteristic length scale parameters for both the crack phase field and the interface phase field are set to be 1.5 times the size of the element $\ell_d = \ell_\beta = 1.5$ m. The external surfaces are mechanically fixed by setting zero displacements, meanwhile the pressure is assumed to be zero such that the fluid flows freely through the external surfaces. The results of the hydraulic fracturing simulation are shown in Fig. 18, where Fig. 18(a)-(d) each depicts the crack phase field $d(t)$ at different times $t = 0, 2, 5, 10$ s and Fig. 18(e) and (f) shows the vertical displacement field and the pressure field on selected slices at $t = 10$ s. From Fig. 18(a)-(d), it can be observed that the initially defined square crack notch gradually grows

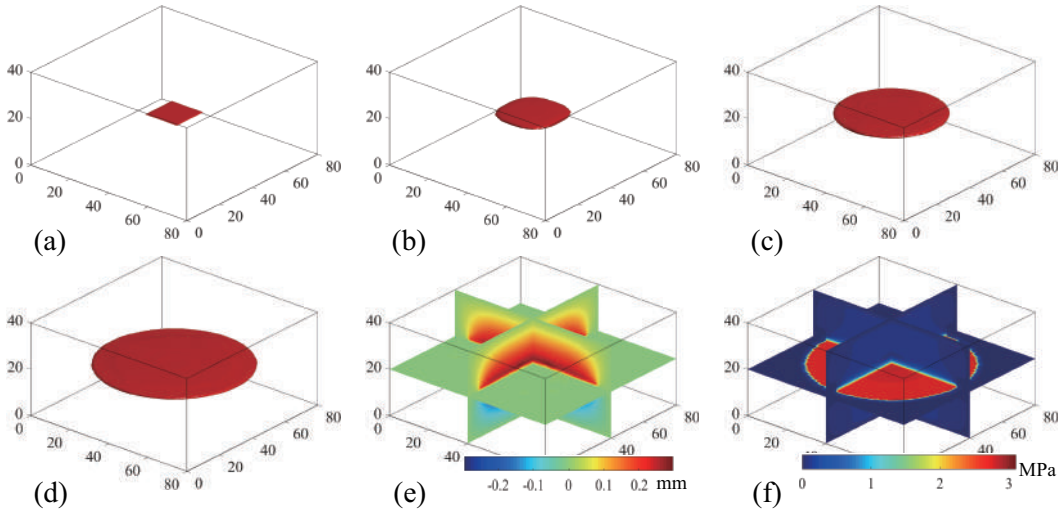

Fig. 18. Hydraulic fracturing simulation of a homogeneous 3D medium subjected to a constant fluid volume injection in the initial crack; crack phase field at (a) $t = 0$ s, (b) $t = 2$ s, (c) $t = 5$ s, (d) $t = 10$ s; (e) vertical displacement field on selected slices at $t = 10$ s; and (f) pressure field on two slices at $t = 10$ s.

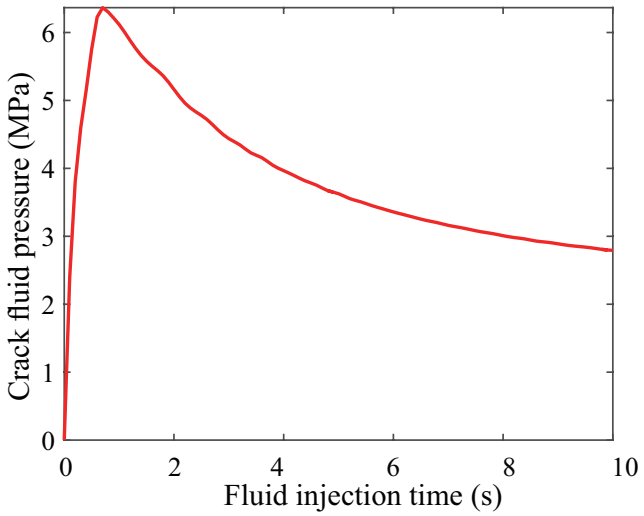

Fig. 19. Fluid pressure within the crack versus injection time during the hydraulic fracturing process of the 3D homogeneous medium .

to a penny-shaped fracture. The fluid pressure within the crack grows quickly before cracking and then gradually reduces to a constant value due to the increased permeability along the cracking direction. These observations are in line with the 2D case considered above in Section 5.1. The maximum fluid pressure within the crack versus the fluid injection time is given in Fig. 19.

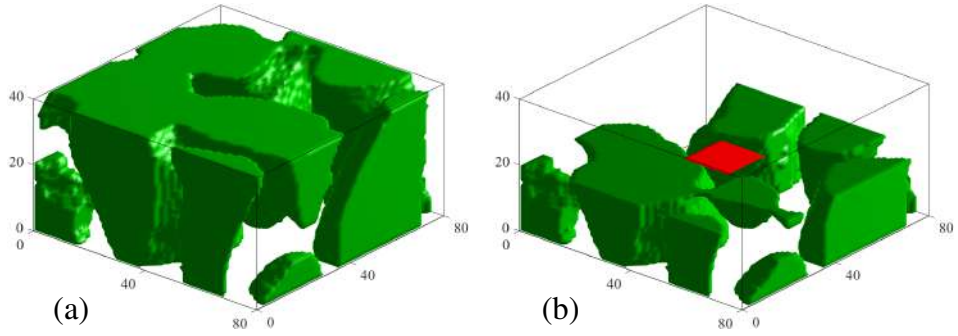

Fig. 20. A highly heterogeneous 3D medium obtained from a microtomography image [39] (a) in green, the geometry of the inclusions; (b) in red, the initial crack.

5.5 Hydraulic fracturing of a 3D heterogeneous medium

In this example, we further investigate the method by simulating hydro-mechanical crack propagation in a 3D heterogeneous medium as shown in Fig. 20. The segmented 3D voxel model has been obtained by X-ray micro-tomography of a light-weight concrete sample [39]. The dimensions of this 3D medium is $80 \times 80 \times 40$ mm^3. The properties of the matrix and inclusions are the same as in the previous example. For interfaces, the model II of the previous example has been used. The mesh matches the voxels of the 3D tomography image consisting in $80 \times 80 \times 40$ eight-node cubic elements. Displacements and fluid pressure are set to zero over the external boundary. A constant fluid flow of 0.6 mm^3/s is injected on a initial crack of surface 16×16 mm^2 located at the center of the domain during 30 s with a constant time step $\Delta t = 0.1$ s. The characteristic length scale parameters for both the crack phase field and the interface phase field are set to $\ell_d = \ell_\beta = 1.5$ mm.

The evolution of the crack phase field during the hydraulic fracturing test is given in Fig. 21. For the purpose of visualization, only the lower half of the 3D medium is shown to better visualize the crack propagation. As can be observed, the initial horizontally defined square crack surface propagates along the interfaces of the surrounding low permeable inclusions. Due to the high heterogeneity of the realistic 3D medium, a very complex crack pattern is created. The pressure fields on two selected slices are also shown in Fig. 21. We can note that the highest fluid pressure is located within the cracks and the pressure quickly decrease outside the cracks because of the low permeability of the matrix.

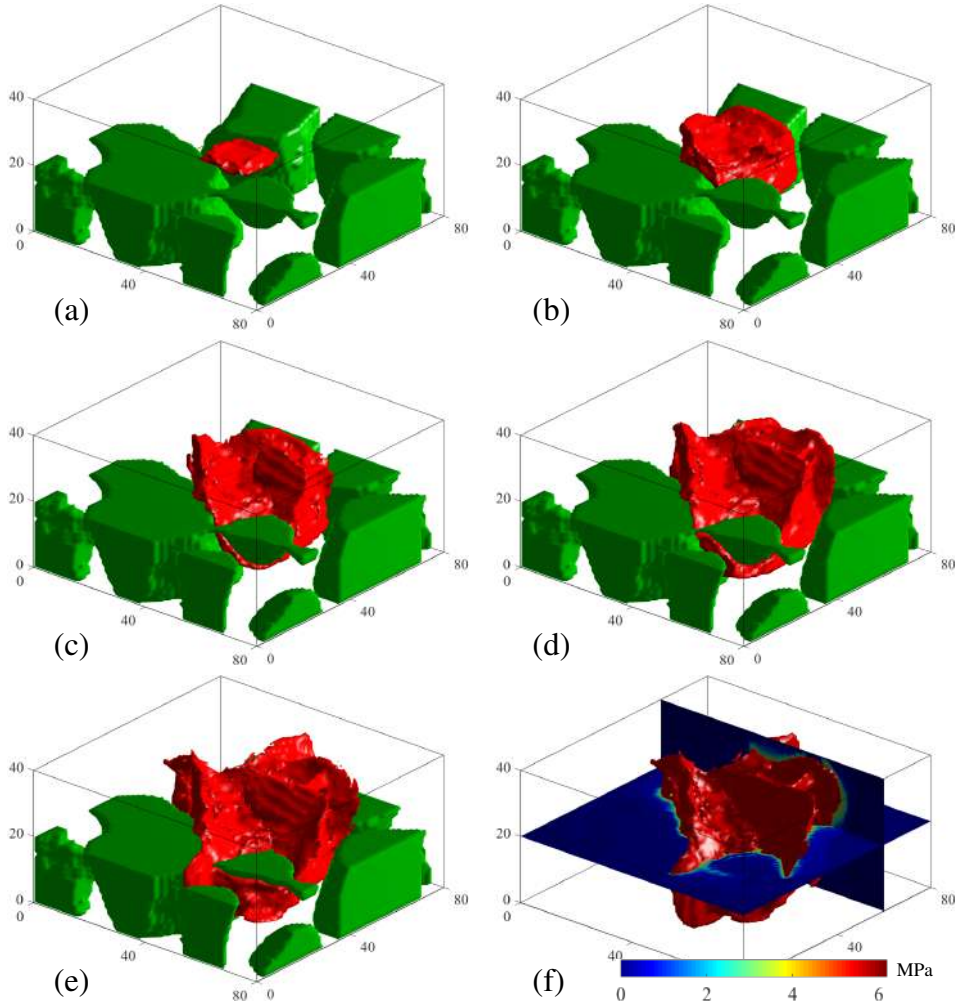

Fig. 21. Evolution of crack phase field during the hydraulic fracturing of the realistic heterogeneous 3D medium at (a) $t = 1$ s, (b) $t = 6$ s, (c) $t = 12$ s, (d) $t = 18$ s, (e) $t = 30$ s and (f) pressure field at $t = 30$s.

6 Conclusion

In this work, we have proposed an extension of the phase field method to hydraulic fracturing to take into account the following features: (a) the presence of heterogeneities; (b) interfacial damage and (c) the possibility to model the initial geometry and the cracks in regular grids of voxels as arising from experimental imaging techniques. For this purpose, we have extended the framework proposed in [42] to hydro-mechanical coupling. In [42], the formulation allowed interaction between bulk cracks and interfacial damage within the phase field and regular meshes for arbitrary morphologies of heterogeneities through an appropriate regularized framework of both interface and bulk crack discontinuities. In the present paper, this framework has been extended to modeling of anisotropic fluid flow within bulk and interfacial cracks and the coupling between the fluid flow within the porous matrix and the crack initiation and

propagation. The obtained framework avoids the burden of remeshing during crack initiation and propagation, is well adapted to simulations within voxel-based models of heterogeneous media as arising from experimental imaging, and does not require internal variables or describing the damage at the interfaces. We have validated the method by a series of benchmark tests and have applied it to hydraulic fracturing of highly heterogeneous media composed of a porous matrix and rigid inclusions with complex geometrical shapes. To our best knowledge, the presented simulations involving hydraulic fracturing, with interfacial damage and realistic voxel-based models of heterogeneous media have been presented here for the first time. Then, the present framework seems to be very promising for predicting initiation, propagation of complex microcracking in a hydro-mechanical context in highly heterogeneous media, such as concrete or geological media.

7 Ackowledgements

This work has benefited from a French government grant managed by ANR within the frame of the national program Investments for the Future ANR-11-LABX-022-01 (LABEX MMCD). JY thanks the financial support of Institut Universitaire de France (IUF).

References

[1] L. Ambrosio and V.M. Tortorelli. Approximation of functional depending on jumps by elliptic functional via γ-convergence. *Communications on Pure and Applied Mathematics*, 43(8):999–1036, 1990.

[2] H. Amor, J.-J. Marigo, and C. Maurini. Regularized formulation of the variational brittle fracture with unilateral contact: Numerical experiments. *J. Mech. Phys. Solids*, 57(8):1209–1229, 2009.

[3] Z.P. Bažant, M. Salviato, V.T. Chau, H. Visnawathan, and A. Zubelewicz. Why fracking works. *Journal of Applied Mechanics, Transactions ASME*, 81(10), 2014.

[4] M. Belmokhtar, P. Delage, S. Ghabezloo, A.M. Tang, H. Menaceur, and N. Conil. Poroelasticity of the callovo–oxfordian claystone. *Rock Mechanics and Rock Engineering*, pages 1–19, 2016.

[5] M.A. Biot. Theory of finite deformations of porous solids. *Indiana University Mathematics Journal*, 21(7):597–620, 1972.

[6] T.J. Boone and A.R. Ingraffea. A numerical procedure for simulation of hydraulically-driven fracture propagation in poroelastic media. *International*

Journal for Numerical and Analytical Methods in Geomechanics, 14(1):27–47, 1990.

[7] M.J. Borden, C.V. Verhoosel, M.A. Scott, T.J.R. Hughes, and C.M. Landis. A phase-field description of dynamic brittle fracture. *Computer Methods in Applied Mechanics and Engineering*, 217-220:77–95, 2012.

[8] B. Bourdin, G.A. Francfort, and J.J. Marigo. The variational approach to fracture. *Journal of elasticity*, 91(1-3):5–148, 2008.

[9] B. Bourdin, J.-J. Marigo, C. Maurini, and P. Sicsic. Morphogen- esis and propagation of complex cracks induced by thermal shocks. *Phys. Rev. Lett.*, 112:014301, 2014.

[10] F. Brezzi and M. Fortin. *Mixed and Hybrid Finite Element Methods*. Springer-Verlag, 1991.

[11] C. Chukwudozie, B. Bourdin, and K. Yoshioka. A variational approach to the modeling and numerical simulation of hydraulic fracturing under in-situ stresses. In *Proceedings of the 38th Workshop on Geothermal Reservoir Engineering*, 2013.

[12] B. Damjanac, C. Detournay, and P.A. Cundall. Application of particle and lattice codes to simulation of hydraulic fracturing. *Comp. Part. Mech.*, 3(2):249–261, 2016.

[13] R. De Borst, J. Réthoré, and M.-A. Abellan. A numerical approach for arbitrary cracks in a fluid-saturated medium. *Archive of Applied Mechanics*, 75(10-12):595–606, 2006.

[14] E. Detournay. Propagation regimes of fluid-driven fractures in impermeable rocks. *International Journal of Geomechanics*, 4(1):35–45, 2004.

[15] G.A. Francfort and J.J. Marigo. Revisiting brittle fracture as an energy minimization problem. *Journal of the Mechanics and Physics of Solids*, 46(8):1319–1342, 1998.

[16] D. Garagash and E. Detournay. The tip region of a fluid-driven fracture in an elastic medium. *Journal of Applied Mechanics, Transactions ASME*, 67(1):183–192, 2000.

[17] S. Ghabezloo and J. Sulem. Stress dependent thermal pressurization of a fluid-saturated rock. *Rock Mechanics and Rock Engineering*, 42(1):1, 2009.

[18] S. Ghabezloo, J. Sulem, and J. Saint-Marc. The effect of undrained heating on a fluid-saturated hardened cement paste. *Cement and Concrete Research*, 39(1):54–64, 2009.

[19] P. Grassl. A lattice approach to model flow in cracked concrete. *Cement Concrete Composites*, 31:454–460, 2009.

[20] P. Grassl, C. Fahy, and D. Gallipoli. On a 2d hydro-mechanical lattice approach for modelling. *Journal of the Mechanics and Physics of Solids*, 75:104–118, 2015.

[21] P. Gupta and C.A. Duarte. Simulation of non-planar three-dimensional hydraulic fracture propagation. *Int. J. Numer. Anal. Meth. Geomech.*, 38:1397–1430, 2014.

[22] V. Hakim and A. Karma. Laws of crack motion and phase-field models of fracture. *Journal of the Mechanics and Physics of Solids*, 57(2):342–368, 2009.

[23] F. Irzal, J.J.C. Remmers, J.M. Huyghe, and R. De Borst. A large deformation formulation for fluid flow in a progressively fracturing porous material. *Computer Methods in Applied Mechanics and Engineering*, 256:29–37, 2013.

[24] S.A. Khristianovic and Y.P. Zheltov. Formation of vertical fractures by means of highly viscous liquid. *in: Proceedings of the Fourth World Petroleum Congress 2*, pages 579–586, 1955.

[25] B. Lecampion and E. Detournay. An implicit algorithm for the propagation of a hydraulic fracture with a fluid lag. *Computer Methods in Applied Mechanics and Engineering*, 196(49-52):4863–4880, 2007.

[26] S. Lee, M.F. Wheeler, and T. Wick. Pressure and fluid-driven fracture propagation in porous media using an adaptive finite element phase field model. *Computer Methods in Applied Mechanics and Engineering*, 305:111–132, 2016.

[27] C. Miehe, M. Hofacker, L.-M. Schanzel, and F. Aldakheel. Phase field modeling of fracture in multi-physics problems. Part II. Coupled brittle-to-ductile failure criteria and crack propagation in thermo-elastic-plastic solids. *Computer Methods in Applied Mechanics and Engineering*, 294:486–522, 2015.

[28] C. Miehe, M. Hofacker, and F. Welschinger. A phase field model for rate-independent crack propagation: Robust algorithmic implementation based on operator splits. *Computer Methods in Applied Mechanics and Engineering*, 199(45-48):2765–2778, 2010.

[29] C. Miehe and S. Mauthe. Phase field modeling of fracture in multi-physics problems. Part III. Crack driving forces in hydro-poro-elasticity and hydraulic fracturing of fluid-saturated porous media. *Computer Methods in Applied Mechanics and Engineering*, 304:619–655, 2016.

[30] C. Miehe, S. Mauthe, and S. Teichtmeister. Minimization principles for the coupled problem of darcy-biot-type fluid transport in porous media linked to phase field modeling of fracture. *Journal of the Mechanics and Physics of Solids*, 82:186–217, 2015.

[31] C. Miehe, L.-M. Schanzel, and H. Ulmer. Phase field modeling of fracture in multi-physics problems. Part I. Balance of crack surface and failure criteria for brittle crack propagation in thermo-elastic solids. *Computer Methods in Applied Mechanics and Engineering*, 294:449–485, 2015.

[32] C. Miehe, F. Welschinger, and M. Hofacker. Thermodynamically consistent phase-field models of fracture: Variational principles and multi-field fe implementations. *International Journal for Numerical Methods in Engineering*, 83:12731311, 2010.

[33] A. Mikelić, M.F. Wheeler, and T. Wick. A phase-field method for propagating fluid-filled fractures coupled to a surrounding porous medium. *SIAM Multiscale Modeling and Simulation*, 13(1):367–398, 2015.

[34] A. Mikelić, M.F. Wheeler, and T. Wick. Phase-field modeling of a fluid-driven fracture in a poroelastic medium. *Computational Geosciences*, 19(6):1171–1195, 2015.

[35] A. Mikelić, M.F. Wheeler, and T. Wick. A quasi-static phase-field approach to pressur- ized fractures. *Nonlinearity*, 28(5):1371–1399, 2015.

[36] T. Mohammadnejad and A.R. Khoei. An extended finite element method for hydraulic fracture propagation in deformable porous media with the cohesive crack model. *Finite Elements in Analysis and Design*, 73:77–95, 2013.

[37] T. Mohammadnejad and A.R. Khoei. Hydro-mechanical modeling of cohesive crack propagation in multiphase porous media using the extended finite element method. *International Journal for Numerical and Analytical Methods in Geomechanics*, 37(10):1247–1279, 2013.

[38] D. Mumford and J. Shah. Optimal approximations by piecewise smooth functions and associated variational problems. *Communications on Pure and Applied Mathematics*, 42(5):577–685, 1989.

[39] T.T. Nguyen, J. Yvonnet, M. Bornert, and C. Chateau. Initiation and propagation of complex 3d networks of cracks in heterogeneous quasi-brittle materials: Direct comparison between in situ testing-microct experiments and phase field simulations. *Journal of the Mechanics and Physics of Solids*, 99:320–350, 2016.

[40] T.T. Nguyen, J. Yvonnet, M. Bornert, C. Chateau, K. Sab, R. Romani, and R. Le Roy. On the choice of parameters in the phase field method for simulating crack initiation with experimental validation. *International Journal of Fracture*, 197:213–226, 2016.

[41] T.T. Nguyen, J. Yvonnet, Q.-Z. Zhu, M. Bornert, and C. Chateau. A phase field method to simulate crack nucleation and propagation in strongly heterogeneous materials from direct imaging of their microstructure. *Engineering Fracture Mechanics*, 139:18–39, 2015.

[42] T.T. Nguyen, J. Yvonnet, Q.-Z. Zhu, M. Bornert, and C. Chateau. A phase-field method for computational modeling of interfacial damage interacting with crack propagation in realistic microstructures obtained by microtomography. *Comput. Meth. Appl. Mech. eng.*, (312):567–595, 2016.

[43] M. Nikolic, A. Ibrahimbegovic, and P. Miscevic. Discrete element model for the analysis of fluid-saturated fractured poro-plastic medium based on sharp crack representation with embedded strong discontinuities. *Computer Methods in Applied Mechanics and Engineering*, 298:407–427, 2016.

[44] J. Réthoré, R. De Borst, and M.-A. Abellan. A two-scale model for fluid flow in an unsaturated porous medium with cohesive cracks. *Computational Mechanics*, 42(2):227–238, 2008.

[45] B.A. Schrefler, S. Secchi, and L. Simoni. On adaptive refinement techniques in multi-field problems including cohesive fracture. *Computer Methods in Applied Mechanics and Engineering*, 195(4-6):444–461, 2006.

[46] S. Secchi and B.A. Schrefler. A method for 3-D hydraulic fracturing simulation. *International Journal of Fracture*, 178(1-2):245–258, 2012.

[47] Richa Shukla, Pathegama Ranjith, Asadul Haque, and Xavier Choi. A review of studies on CO^2 sequestration and caprock integrity. *Fuel*, 89(10):2651–2664, 2010.

[48] D.A. Spence and P. Sharp. Self-similar solutions for elastohydrodynamic cavity flow. *Proceedings of The Royal Society of London, Series A: Mathematical and Physical Sciences*, 400(1819):289–313, 1985.

[49] M.J. van den Bosch, P.J.G. Schreurs, and M.G.D. Geers. An improved description of the exponential xu and needleman cohesive zone law for mixed-mode decohesion. *Engineering Fracture Mechanics*, 73(9):1220 – 1234, 2006.

[50] C.V. Verhoosel and R. de Borst. A phase-field model for cohesive fracture. *International Journal for Numerical Methods in Engineering*, 96(1):43–62, 2013.

[51] M. Wang and Y.T. Feng anf C.Y. Wang. Numerical investigation of initiation and propagation of hydraulic fracture using the coupled bonded particle-lattice bolzmann method. *Comput. Struct.*, 181:32–40, 2017.

[52] Y. Wang and D. Adhikary. Hydraulic fracture simulation based on coupled discrete element method and lattice bolzmann method. In *Proceeding World Geothermal Congress*, 2015.

[53] M.F. Wheeler, T. Wick, and W. Wollner. An augmented-lagrangian method for the phase-field approach for pressurized fractures. *Computer Methods in Applied Mechanics and Engineering*, 271:69–85, 2014.

[54] T. Wick. Coupling fluid-structure interaction with phase-field fracture. *J. Comput. Phys.*, 327:67–96, 2016.

[55] Y Zheng, R Burridge, and DR Burns. Reservoir simulation with the finite element method using biot poroelastic approach. Technical report, Massachusetts Institute of Technology. Earth Resources Laboratory, 2003.

[56] O.C. Zienkiewicz, R. Taylor, and J.Z. Zhu. *The Finite Element Methods*. Elsevier, 2005.